

Banner appropriate to article type will appear here in typeset article

# Plasma kinetics: Discrete Boltzmann modelling and Richtmyer-Meshkov instability

Jiahui Song<sup>1,2</sup>, Aiguo Xu<sup>2,3,4†</sup>, Long Miao<sup>1‡</sup>, Feng Chen<sup>5</sup>, Zhipeng Liu<sup>6</sup>, Lifeng Wang<sup>2,3</sup>, Ningfei Wang<sup>1</sup>, and Xiao Hou<sup>1</sup>

<sup>1</sup>School of Aerospace Engineering, Beijing Institute of Technology, Beijing, 100081, PR China

<sup>2</sup>Laboratory of Computational Physics, Institute of Applied Physics and Computational Mathematics, Beijing 100088, PR China

<sup>3</sup>HEDPS, Center for Applied Physics and Technology, and College of Engineering, Peking University, Beijing 100871, PR China

<sup>4</sup>State Key Laboratory of Explosion Science and Technology, Beijing Institute of Technology, Beijing 100081, PR China

<sup>5</sup>School of Aeronautics, Shandong Jiaotong University, Jinan 250357, PR China

<sup>6</sup>Department of Physics, School of Science, Tianjin Chengjian University, Tianjin, 300384, PR China

(Received xx; revised xx; accepted xx)

A discrete Boltzmann model (DBM) for plasma kinetics is proposed. The DBM contains two physical functions. The first is to capture the main features aiming to investigate and the second is to present schemes for checking thermodynamic non-equilibrium (TNE) state and describing TNE effects. For the first function, mathematically, the model is composed of a discrete Boltzmann equation coupled by a magnetic induction equation. Physically, the model is equivalent to a hydrodynamic model plus a coarse-grained model for the most relevant TNE behaviors including the entropy production rate. The first function is verified by recovering hydrodynamic non-equilibrium (HNE) behaviors of a number of typical benchmark problems. Extracting and analyzing the most relevant TNE effects in Orszag-Tang problem are practical applications of the second function. As a further application, the Richtmyer-Meshkov instability with interface inverse and re-shock process is numerically studied. It is found that, in the case without magnetic field, the non-organized momentum flux shows the most pronounced effects near shock front, while the non-organized energy flux shows the most pronounced behaviors near perturbed interface. The influence of magnetic field on TNE effects shows stages: before the interface inverse, the TNE strength is enhanced by reducing the interface inverse speed; while after the interface inverse, the TNE strength

† Email address for correspondence: Xu\_Aiguo@iapcm.ac.cn

‡ Email address for correspondence: miaolong@bit.edu.cn

is significantly reduced. Both the global averaged TNE strength and entropy production rate contributed by non-organized energy flux can be used as physical criteria to identify whether or not the magnetic field is sufficient to prevent the interface inverse.

**Key words:** plasma kinetic; magnetohydrodynamic; Richtmyer-Meshkov instability

---

**MSC Codes** (*Optional*) Please enter your MSC Codes here

## 1. Introduction

As the fourth state of matter, plasma exists extensively in natural and various industrial fields such as initial confinement fusion (ICF) (Betti & Hurricane 2016; Abu-Shawareb *et al.* 2022). In ICF, the target pellet is driven by strong laser or x ray, which ionizes the shell ablator material and forms strong shock waves to compress the fuel centrally to a high temperature and density of the ignition state. When the imposing shock wave passes through a perturbed interface, the perturbation amplitude increases with time, resulting in the mix of ablator material into the fuel plasmas and even causing ignition failure (Brouillette 2002). This phenomenon was first investigated theoretically by Richtmyer; (1960) through linear stability analysis, then qualitatively verified by Meshkov (1969) through shock tube experiments. Now, it is generally referred to as the Richtmyer-Meshkov instability (RMI). As a physical phenomenon that is bound to occur when certain conditions are met, the RMI also plays important roles in astrophysics (Arnett 2000; Sano *et al.* 2021), shock wave physics, combustion (Khokhlov *et al.* 1999) and other kinds of systems (Zhou 2017a,b; Zhou *et al.* 2021).

Due to the importance and complexity of RMI, extensive theoretical, experimental and numerical studies have been carried out (Zhai *et al.* 2011; Xu *et al.* 2016; Lei *et al.* 2017; Zhou 2017a,b; Wang *et al.* 2017; Zhai *et al.* 2018). Among them, plasma RMI is one of the important research areas. Previous theoretical and numerical studies for plasma RMI are mainly based on two kinds of models. The first kinds are various magnetohydrodynamics (MHD) models which simultaneously couple Euler/Navier-Stokes (NS) equations with Maxwell equations. Based on MHD models, the effects of applied magnetic fields and self-generated electromagnetic fields on the development of plasma RMI have been extensively studied (Samtaney 2003; Wheatley *et al.* 2005a,b; Cao *et al.* 2005; Qiu *et al.* 2008; Wheatley *et al.* 2009; Sano *et al.* 2012, 2013; Wheatley *et al.* 2014; Mostert *et al.* 2015, 2017; Bond *et al.* 2017b; Zhang *et al.* 2020; Qin & Dong 2021; Li *et al.* 2022b; Bakhsh 2022; Zhang *et al.* 2023; Tapinou *et al.* 2023). It should be noted that, the MHD models based on continuum hypothesis are only valid when Knudsen number  $Kn$  (defined as the ratio of molecular mean free path  $l$  to a characteristic length scale  $L$ ) is sufficient small. However, the local  $Kn$

near the imposing plasma shock (Vidal *et al.* 1993; Liu *et al.* 2022; Bond *et al.* 2017a) and perturbed interface is generally so large that it challenges the validity of the continuum assumption (McMullen *et al.* 2022), resulting in inaccurate predictions of physical quantities (Gan *et al.* 2013; Zhang *et al.* 2019b,a; Qiu *et al.* 2021; Gan *et al.* 2022). Besides, a considerable part of the MHD models neglect the particle collision, while Robey (2004); Rinderknecht *et al.* (2018); Cai *et al.* (2020); Yao *et al.* (2020); Cai *et al.* (2021); Shan *et al.* (2021) point out that the kinetic effects caused by particle collisions have the potential to impact the ICF. In order to address the above limitations, the second kinds of models based on the non-equilibrium statistical physics are promising, which are often referred to as the kinetic methods. Boltzmann equation is one of the most fundamental and widely used kinetic equations. Based on Boltzmann equation, kinetic methods which consider particle collision have been rapidly developed, such as Direct simulation Monte Carlo (DSMC) (Bird 1998), gas-kinetic unified algorithms (GKUA) (Li *et al.* 2015), unfinied gas-kinetic scheme (UGKS) (Xu & Huang 2010; Liu & Xu 2017), lattice Boltzmann method (LBM) (Chen *et al.* 1991; Wagner & Yeomans 1998; Succi 2001; Sofonea & Sekerka 2003; Dellar 2002; Sofonea *et al.* 2004; Pattison *et al.* 2008; Li *et al.* 2016, 2012; Ledesma-Aguilar *et al.* 2014; Chen *et al.* 2018b; Wang *et al.* 2020; De Rosis *et al.* 2021a,b; Huang *et al.* 2021; Czelusniak *et al.* 2022), particle-in-cell (PIC) (Ji & Held 2013; Asahina *et al.* 2017), hybrid fluid-PIC (Cai *et al.* 2021) and Vlasov-Fokker-Planck (VFP) method (Larroche *et al.* 2016; Keenan *et al.* 2017), etc. Some of these methods have provided a promising solution for studying the RMI (Meng *et al.* 2019; Kumar & Maheshwari 2020; Liu *et al.* 2020; Yan *et al.* 2021).

When considering particle collisions, the temporal and spatial scales in plasma RMI system are more abundant, forming complex hydrodynamic non-equilibrium (HNE) and thermodynamic non-equilibrium (TNE) behaviors. The HNE refers to the non-equilibrium that could be described by hydrodynamic theory. The TNE refers to the non-equilibrium described by kinetic theory and due to that the distribution function  $f$  deviates from its corresponding equilibrium distribution function  $f^{eq}$ . It is clear that the HNE is only a small portion of the TNE (Xu & Zhang 2022). In fact, the insufficient particle collision frequency causes the system to deviate from its local thermodynamic equilibrium state, leading to complex non-equilibrium behaviors such as diffusion, viscosity and heat conduction. Thus, the accurate extraction and analysis of TNE is of substantial importance for evaluating the kinetic effects.

From the point view of continuum, the  $Kn$  can be regarded as the rescaled averaged particle spacing, which characterizes the degree of non-continuum (or discreteness). From the point view of TNE, the  $Kn$  can be regarded as the rescaled thermodynamic relaxation time, which characterizes the degree of TNE of the system. Thus, for the shock wave and perturbed interface where  $Kn$  is high in plasma RMI, the system may deviate significantly from its local thermodynamic equilibrium state. When the kinetic effects are strong, without considering TNE, the physical quantities such as density, temperature, pressure, heat flux and viscous stress will have significantly deviation (Lin & Luo 2019; Chen *et al.* 2020; Gan

*et al. 2018*), and the heat flux and viscous stress may even be wrong in direction (*Zhang et al. 2019a*). Even for the case where the  $Kn$  is small enough and consequently the NS description is reasonable, the NS shows deficiency or inconvenience for investigating some TNE behaviors, such as how the various TNE mechanisms influence the entropy production rates. Nowadays, TNE is attracting more attention with time (*Chen & Zhao 2017; Qiu et al. 2020, 2021; Bao et al. 2022*), but is still far from being fully understood.

In order to extract and analyze TNE, the deviation between  $f$  and  $f^{eq}$  needs to be quantified. According to Chapman-Enskog (CE) multi-scale analysis, the macroscopic hydrodynamic equations can be regarded as the conservation moments equation of Boltzmann equation near the continuum and thermodynamic equilibrium state. Since the current MHD models and mesoscopic kinetic methods mentioned above only consider the conservation moments of  $f$ , which corresponding to mass, momentum and energy conservation, many TNE information which are helpful for physical understanding the underlying fluid kinetic are not available through the above MHD and kinetic methods. In recent years, Xu's group (*Xu et al. 2018; Lai et al. 2016; Chen et al. 2016; Lin et al. 2017; Chen et al. 2018a; Ye et al. 2020; Chen et al. 2020; Lin et al. 2021; Xu et al. 2021a,c,d; Chen et al. 2022b,a; Li et al. 2022c*) has developed a new physical modelling and analysis method, that is the discrete Boltzmann method (DBM). Besides being able to recover the corresponding hydrodynamic model described by the Navier-Stokes, Burnett or super-Burnett equations, the core of the second function of DBM is to use the physical quantities defined by non-conserved moments of  $(f - f^{eq})$  to extract TNE effects. The non-conserved moments here refer to higher-order kinetic moments other than mass, momentum and energy moments. The starting point of DBM and very basic understanding are that with increasing the non-continuity and TNE, the complexity of system behaviors increases sharply, and more physical quantities are needed to describe the state and behaviors. According to the CE theory, *with the increase of  $Kn$ , the non-significant decrease of the system state and behavior description function requires the introduction of more non-conserved moments* (*Xu et al. 2018, 2021a,c,d*). Until now, nearly all existing DBM methods are for neutral fluids (*Lai et al. 2016; Chen et al. 2016; Lin et al. 2017; Chen et al. 2018a; Ye et al. 2020; Chen et al. 2020; Lin et al. 2021; Chen et al. 2022a; Li et al. 2022c; Chen et al. 2022b; Li et al. 2022a*), while the temporal and spatial scales in the plasma RMI are more abundant, forming complex HNE and TNE behaviors.

In this paper, the DBM coupling the effects of electromagnetic fields is constructed and further applied to study the RMI in plasma system. The paper is arranged as follows. The state of art for plasma kinetics is reviewed in Section I, where two problems, (i) how to simulate and (ii) how to analyze the kinetic behaviors, are addressed. Specifically, the two problems are as follows: (i) how to simulate the main kinetic features aiming to investigate, and (ii) how to check the TNE state, describe the corresponding effect and extract more information having potential applications. The framework for constructing a single-distribution-function (SDF) DBM is formulated in Section II. The SDF DBM corresponds to the single-fluid MHD model where only one set of hydrodynamic quantities are used. The DBM is beyond

the MHD model from the sense that it has more physical functions than the latter. In Section III, some HNE behaviors of a number of typical benchmark problems are used to validate the first function of the DBM, and then the TNE behaviors of Orszag-Tang vortex problem are studied. In Section IV, the HNE and TNE behaviors of RMI with and without initial applied magnetic field are investigated. At last, the conclusion and discussions are given in Section V.

## 2. Physical models

In this section, the differences in research ideas between DBM and LBM are first discussed. Then, three main steps for constructing DBM are presented in detail, including two coarse-grained physical modelling steps and a step to extract and measure non-equilibrium effects. Furthermore, we introduce a model describing the evolution of the electromagnetic field and explain in detail how this model and the DBM are coupled.

### 2.1. Discrete Boltzmann Model

LBM is one of the fastest-growing and most widely-used kinetic methods in recent years (Succi 2001). The LBM studies have two different branches. The first branch aims to work as a novel discrete format for numerical solving hydrodynamic equations or other kinds of partial differential equations (PDE). The second aims to work as a new method for constructing kinetic models of complex flows (Succi 2001; Xu & Zhang 2022; Gan *et al.* 2022). The vast majority of LBM methods in the current literature belong to the first branch. As a numerical solution method, the first branch of LBM should be loyal to the corresponding original model. The numerical accuracy and efficiency are its main concerns. At present, a variety of LBM models for solving magnetohydrodynamic equations have been developed and used (Dellar 2002; Pattison *et al.* 2008; De Rosiis *et al.* 2021*b,a*).

DBM is a modelling and analysis method developed from the second branch of LBM working as a physical model construction method. DBM aims at the two problems. The first is how to describe, and the second is how to analyse the flow behaviors. It breaks through the continuity and near-equilibrium assumptions of traditional macroscopic modelling methods, no longer uses the lattice gas image of standard LBM, and adds methods based on phase space for checking, exhibiting, describing and analyzing the non-equilibrium state and effect. A DBM is equivalent to a hydrodynamic model plus a coarse-grained model for the most relevant TNE behaviors. Besides the hydrodynamic model described by the Euler, NS, Burnett equations, etc., *the appearance of second function of DBM, the coarse-grained model for describing the most relevant TNE effects, is an inevitable requirement for the description and control of non-equilibrium and discrete behaviors.* As the degree of non-continuity and non-equilibrium increases, more physical quantities are used to describe the state and behavior of the system, which is a typical feature of DBM that differs from traditional modelling methods. From the perspective of kinetic macro modelling (KMM), it is a requirement of obtaining

the more accurate constitutive relations; From the perspective of kinetics theory, it is a requirement of obtaining the more accurate distribution function. Different perspectives lead to the same destination (Xu & Zhang 2022). According to the research needs, DBM grasps the main contradiction, selects a perspective, and studies a set of kinetic properties of the system. Therefore, it requires that the calculation results of the kinetic moments describing this set of kinetic properties cannot be changed due to model simplification. Then, with time, more schemes are introduced to check the TNE state, extract the TNE information and describe corresponding TNE effects (Xu *et al.* 2012, 2015, 2021*d,b*).

From Boltzmann equation to DBM, for bulk flow, three basic steps are needed: (i) Modification and simplification of the Boltzmann equation, (ii) discretization of the particle velocity space, (iii) extraction and measurement of non-equilibrium effects. Among them, the first two steps are the coarse-grained physical modelling process, which aim is to build a simple physical model with sufficient physical functions to meet the problem research. The third step is the core of the second function of DBM, and its purpose is to quickly and effectively extract non-equilibrium effects with the help of non-conserved kinetic moments. In addition, it should be emphasized that the above three steps are aimed at the fluid far away from the wall. For near-wall fluids where the boundary effects needs to be considered, appropriate kinetic boundary conditions must be introduced (Zhang *et al.* 2018, 2022*b*).

### 2.1.1. *Modification and simplification of the Boltzmann equation*

As one of the most basic model equations in non-equilibrium statistical physics, the origin Boltzmann equation has the ability to describe the whole flow regimes (from continuous flow to free molecular flow) and different extent of non-equilibrium effects (from quasi-equilibrium to non-equilibrium flows). However, the high-dimensional integral collision term on the right hand of Boltzmann equation is too complicated to solve, which brings inconvenience to practical research. In order to simplify the collision term, a convenient and effective way is to introduce a equilibrium distribution function  $f^{eq}$  and write the Boltzmann collision term into the form of a linearized collision operator as follows,

$$\frac{\partial f}{\partial t} + \mathbf{v} \cdot \frac{\partial f}{\partial \mathbf{r}} + \mathbf{a} \cdot \frac{\partial f}{\partial \mathbf{v}} = -\frac{1}{\tau} (f - f^{eq}), \quad (2.1)$$

where  $f$  and  $f^{eq}$  are the distribution function and equilibrium distribution function, respectively. The variables  $\mathbf{r}$ ,  $\mathbf{v}$ ,  $\mathbf{a}$ ,  $t$ ,  $\tau$  are the particle space coordinate, velocity, acceleration caused by external force, time and relaxation time, respectively. This simplification method is based on the following physical basis: Assuming that the details and effects of a specific collision have no obvious influence on the main characteristics of the collision term when describing a fluid system, so we can obtain the main characteristics of the collision term by statistically averaging the effects of all collisions. Here, the average effect of particle collisions is to make  $f$  gradually evolves towards  $f^{eq}$ , and the speed of this process is controlled by relaxation time  $\tau$ . The above form was first proposed by Bhatnagar, Gross, and Krook, so it is also known as Boltzmann-BGK model (Bhatnagar *et al.* 1954).

At present, BGK-like models such as the BGK model, ES-BGK model, Shakov model, and Rykov model have been widely used in various kinetic methods. It should be emphasized that the original BGK model only preserves the mass/momentum/energy conservation and the  $H$ -theorem, which means the original BGK model only suits for the system that is always in local quasi-equilibrium state. However, as  $Kn$  increases, small structures and fast modes appear, and real system tends to deviate significantly from the equilibrium state. It is clear that the BGK in various kinetic methods is surely not the original BGK. It is actually a simplified model combining the kinetic theory and mean field theory (Xu & Zhang 2022; Gan *et al.* 2022). Here, the BGK model is adopted, and the form of  $f^{eq}$  is as follows,

$$f^{eq}(\rho, \mathbf{u}, T) = \rho \left( \frac{1}{2\pi RT} \right)^{D/2} \left( \frac{1}{2\pi nRT} \right)^{1/2} \exp \left[ -\frac{(\mathbf{v} - \mathbf{u})^2}{2RT} - \frac{\eta^2}{2nRT} \right], \quad (2.2)$$

where  $\rho$ ,  $\mathbf{u}$ ,  $T$ ,  $R$  are density, bulk velocity, temperature and gas constant, respectively.  $D$  is the number of space dimension, and  $n$  is the number of extra degrees of freedom, with which the specific heat ratio is  $\gamma = (D + n + 2)/(D + n)$ .  $\eta$  is a free parameter that describes the energy of extra degrees of freedom including molecular rotation and vibration inside the molecules.

According to the theory of mesoscopic non-equilibrium statistical physics, all the information of system during evolution is contained in the distribution function  $f$ , and the corresponding macroscopic physical quantities can be obtained by taking the kinetic moments of  $f$ . Here, two sets of kinetic moments are defined as follows:

$$\mathbf{M}_{m,n}(f) = \int_{-\infty}^{\infty} \left( \frac{1}{2} \right)^{1-\delta_{m,n}} (f) \underbrace{\mathbf{v}\mathbf{v} \cdots \mathbf{v}}_n (\mathbf{v} \cdot \mathbf{v})^{(m-n)/2} d\mathbf{v}, \quad (2.3)$$

$$\mathbf{M}_{m,n}^*(f) = \int_{-\infty}^{\infty} \left( \frac{1}{2} \right)^{1-\delta_{m,n}} (f) \underbrace{\mathbf{v}^*\mathbf{v}^* \cdots \mathbf{v}^*}_n (\mathbf{v}^* \cdot \mathbf{v}^*)^{(m-n)/2} d\mathbf{v}, \quad (2.4)$$

where  $\delta_{m,n}$  is the Kronecker delta function. The subscript  $m, n$  represents the  $m$ th-order tensors contracted to  $n$ th-order ones. When  $m = n$ ,  $\mathbf{M}_{m,n}$  and  $\mathbf{M}_{m,n}^*$  are referred to as  $\mathbf{M}_m$  and  $\mathbf{M}_m^*$ .  $\mathbf{v}^* = \mathbf{v} - \mathbf{u}$  represents the thermal fluctuation velocity of particles relative to bulk velocity  $\mathbf{u}$ . Through constructing kinetic moments  $\mathbf{M}_0$ ,  $\mathbf{M}_1$ , and  $\mathbf{M}_{2,0}$  on both sides of Eq (2.1), the generalized hydrodynamic equations<sup>†</sup> could be obtained as follows,

$$\frac{\partial \rho}{\partial t} + \nabla \cdot (\rho \mathbf{u}) = 0, \quad (2.5)$$

$$\frac{\partial \rho \mathbf{u}}{\partial t} + \nabla \cdot (\rho \mathbf{u} \mathbf{u} + \Delta_2) = 0, \quad (2.6)$$

$$\frac{\partial E_T}{\partial t} + \nabla \cdot [E_T \mathbf{u} + \Delta_{3,1}] = 0, \quad (2.7)$$

<sup>†</sup> where the viscous stress and heat conduction may contain not only the contribution of  $f^{(1)}$ , among which the NS viscous stress and NS heat conduction are the simplest cases

where  $E_T = \rho e + \rho u^2/2$  is the total energy, and  $e$  is the energy density.  $\Delta_2$  and  $\Delta_{3,1}$  are two non-equilibrium quantities. For the convenience of discussion, we first give two kinds of definitions of non-equilibrium quantities, as follows,

$$\Delta_{m,n} = \mathbf{M}_{m,n} (f - f^{eq}) = \int_{-\infty}^{\infty} \left(\frac{1}{2}\right)^{1-\delta_{m,n}} \left(f^{(1)} + f^{(2)} + \dots\right) \underbrace{\mathbf{v}\mathbf{v}^* \dots \mathbf{v}}_n (\mathbf{v} \cdot \mathbf{v})^{(m-n)/2} d\mathbf{v}, \quad (2.8)$$

$$\Delta_{m,n}^* = \mathbf{M}_{m,n}^* (f - f^{eq}) = \int_{-\infty}^{\infty} \left(\frac{1}{2}\right)^{1-\delta_{m,n}} \left(f^{(1)} + f^{(2)} + \dots\right) \underbrace{\mathbf{v}^*\mathbf{v}^* \dots \mathbf{v}^*}_n (\mathbf{v}^* \cdot \mathbf{v}^*)^{(m-n)/2} d\mathbf{v}. \quad (2.9)$$

When  $m = n$ , the  $\Delta_{m,n}$  and  $\Delta_{m,n}^*$  are also referred to as  $\Delta_m$  and  $\Delta_m^*$ . For the convenience of discussion,  $\Delta_{m,n}$  is called the non-central moment, and the non-equilibrium information it describes is referred to as thermo-hydrodynamic non-equilibrium (THNE).  $\Delta_{m,n}^*$  is called the central moment, and the non-equilibrium information it describes is referred to as TNE. Parts of the relationship between THNE and TNE are given in reference (Gan *et al.* 2022) as follows,

$$\Delta_2 = \Delta_2^*, \quad (2.10)$$

$$\Delta_{3,1} = \Delta_{3,1}^* + \Delta_2^* \cdot \mathbf{u}. \quad (2.11)$$

Here,  $\Delta_2^*$  is defined as non-organized momentum flux (NOMF), and  $\Delta_{3,1}^*$  is defined as non-organized energy flux (NOEF). Compared with the constitutive of viscous stress and heat flux in NS, Burnett and Super-Burnett equations,  $\Delta_2^*$  and  $\Delta_{3,1}^*$  contain the most complete constitutive information. Thus,  $\Delta_2^*$  and  $\Delta_{3,1}^*$  are also referred to as generalized viscous stress and heat flux. However, the specific forms of  $\Delta_2^*$  and  $\Delta_{3,1}^*$  are basically unknown. To get the specific forms of  $\Delta_2^*$  and  $\Delta_{3,1}^*$ , we need to determine the order of  $f$  to be retained (or the number of kinetic moments to be preserved) through CE multi-scale analysis. The form of CE multi-scale analysis is as follows,

$$f = f^{(0)} + Kn f^{(1)} + Kn^2 f^{(2)} + Kn^3 f^{(3)} + \dots, \quad (2.12)$$

$$\frac{\partial}{\partial t} = Kn \frac{\partial}{\partial t_1} + Kn^2 \frac{\partial}{\partial t_2} + \dots, \quad (2.13)$$

$$\frac{\partial}{\partial \mathbf{r}} = Kn \frac{\partial}{\partial \mathbf{r}_1}, \quad (2.14)$$

where  $f^{(0)} = f^{eq}$ . Here, the zero-order expansions of the time and space derivatives  $\partial/\partial t_0$  and  $\partial/\partial \mathbf{r}_0$  are neglected, for the subscript 0 represents the scale of system and the internal change of system cannot be observed through system scale. Besides, the time is expanded to the second-order and the space is expanded to the first-order. Through this way, the derived equations are exactly the hydrodynamic equations currently used such as NS and Burnett, etc. Theoretically, it is also optional to expand time to the first-order and expand space to the second-order. As long as the derivation process is correct, the obtained hydrodynamic

equations are also correct. Substituting Eqs. (2.12)-(2.14) into Eq. (2.1), and retaining the same order terms of  $Kn$  numbers, we get,

$$Kn^1 : \frac{\partial f^{(0)}}{\partial t_1} + \frac{\partial (f^{(0)} \mathbf{v})}{\partial \mathbf{r}_1} = -\frac{1}{\tau} f^{(1)}, \quad (2.15)$$

$$Kn^2 : \frac{\partial f^{(0)}}{\partial t_2} + \frac{\partial f^{(1)}}{\partial t_1} + \frac{\partial (f^{(1)} \mathbf{v})}{\partial \mathbf{r}_1} = -\frac{1}{\tau} f^{(2)}. \quad (2.16)$$

By taking the  $\mathbf{M}_0$ ,  $\mathbf{M}_1$ , and  $\mathbf{M}_{2,0}$  moments simultaneously on both sides of Eq. (2.15) and use the relation  $f^{(1)} = -\tau [\partial f^{(0)}/\partial t_1 + \partial (f^{(0)} \mathbf{v})/\partial \mathbf{r}_1]$ , the viscous stress and heat flux in NS level can be deduced after performing some mathematical transformations, as follows (Gan *et al.* 2022),

$$\Delta_{2,NS}^* = \Delta_2^{*(1)} = \int_{-\infty}^{\infty} f^{(1)} \mathbf{v}^* \mathbf{v}^* d\mathbf{v} = -\mu [(\nabla \mathbf{u}) + (\nabla \mathbf{u})^T], \quad (2.17)$$

$$\Delta_{3,1,NS}^* = \Delta_{3,1}^{*(1)} = \int_{-\infty}^{\infty} \frac{1}{2} f^{(1)} \mathbf{v}^* \cdot \mathbf{v}^* \mathbf{v}^* d\mathbf{v} = -\kappa \nabla T, \quad (2.18)$$

where  $\mu = \tau \rho RT$  is the viscosity coefficient and  $\kappa = 2\tau \rho RT$  is the heat conductivity. Similarly, the viscous stress  $\Delta_2^{*(2)}$  and heat flux  $\Delta_{3,1}^{*(2)}$  contributed by  $f^{(2)}$  can be deduced from Eq. (2.16), and the viscous stress and heat flux in Burnett level are  $\Delta_{2,Burnett}^* = \Delta_2^{*(1)} + \Delta_2^{*(2)}$  and  $\Delta_{3,1,Burnett}^* = \Delta_{3,1}^{*(1)} + \Delta_{3,1}^{*(2)}$ , respectively. It should be noted that, CE gives the dependence of  $(n+1)$ -th order distribution function  $f^{(n+1)}$  on the  $n$ -th order distribution function  $f^{(n)}$ , and finally gives the dependence of  $f^{(n+1)}$  on  $f^{(0)}$ , where  $f^{(0)}$  is the only one whose kinetic moments are known and can be relied upon in the modelling process. In the derivation of the first-order constitutive relations in NS, the highest-order kinetic moment used is  $\mathbf{M}_{4,2}$ . As for the derivation of the second-order constitutive relations in Burnett, the highest-order kinetic moment used is  $\mathbf{M}_{5,3}$ .

There exist two kinds of methods to obtain the macroscopic hydrodynamic equations. The first is the traditional macroscopic direct modelling method which is based on the continuum assumption and near equilibrium approximation. The second is the KMM method, that is, starting from kinetic equations, to derive the corresponding macroscopic hydrodynamic equations via CE multi-scale analysis. Due to different research ideas, KMM is divided into two categories. The first category follows the traditional modelling idea which concerns only the evolution equations of the conserved kinetic moments, that are, the density, momentum and energy. The second category realizes the insufficiency of the first category in capturing the system behaviors for the high  $Kn$  cases and consequently derives also the evolution equations of the most relevant non-conserved kinetic moments (Chen & Zhao 2017). For convenience of description, we refer the model equations derived from the second category of KMM to as extended hydrodynamic equations (EHE)<sup>†</sup>. Currently, most of the KMM studies belong to the first category.

<sup>†</sup> where the model equations include not only the evolution equations of density, momentum and energy, but also those of the most relevant non-conserved kinetic moments

In contrast, the DBM is a kinetic direct modelling method (KDM). Here ‘direct’ means without needing to know the specific EHE. Because the current DBM is still working in the case where the CE theory is valid, the CE theory is the mathematical guarantee for rationality and effectiveness of DBM. DBM is responsible for the following two aspects: (i) According to the discrete, non-equilibrium degree (described by Knudsen number), determine the system behavior needs to be grasped from what aspects, so as to determine which kinetic moments must be preserved in the process of model simplification, (ii) based on the non-conserved moments of  $(f - f^{eq})$ , present as many as possible schemes for the detection, description, presentation and analysis of the TNE state and effect. For the first aspect, from the perspective of KMM, DBM determines the kinetic moments of  $f^{eq}$  that need to be preserved according to the requirements to obtain the more accurate constitutive expressions; from the perspective of kinetic theory, DBM determines the kinetic moments of  $f^{eq}$  that need to be preserved according to the requirements to obtain the more accurate distribution function expressions (Xu & Zhang 2022). Obviously, the second category of KMM is closest to DBM in physical function.

In addition to the equations for the conservation of mass, momentum, and energy, the extended hydrodynamic equations derived through KMM also includes equations describing the evolution of non-equilibrium quantities such as viscous stress and heat flux. For example, by integrating  $\mathbf{v}^* \mathbf{v}^*$  and  $\frac{1}{2} \mathbf{v}^* \cdot \mathbf{v}^* \mathbf{v}^*$  on both sides of Eq. (2.1) and ignore the external force term, we obtain the following equation (Gan *et al.* 2022),

$$\frac{\partial \Delta_2^*}{\partial t} + \frac{\partial \mathbf{M}_2^*(f^{(0)})}{\partial t} + \nabla \cdot \left[ \mathbf{M}_3^*(f^{(0)}) + \mathbf{M}_2^*(f^{(0)}) \mathbf{u} + \Delta_3^* + \Delta_2^* \mathbf{u} \right] = -\frac{1}{\tau} \Delta_2^*, \quad (2.19)$$

$$\frac{\partial \Delta_{3,1}^*}{\partial t} + \frac{\partial \mathbf{M}_{3,1}^*(f^{(0)})}{\partial t} + \nabla \cdot \left[ \mathbf{M}_{4,2}^*(f^{(0)}) + \mathbf{M}_{3,1}^*(f^{(0)}) \mathbf{u} + \Delta_{4,2}^* + \Delta_{3,1}^* \mathbf{u} \right] = -\frac{1}{\tau} \Delta_{3,1}^*, \quad (2.20)$$

where Eqs. (2.19) and (2.20) describe the evolution of viscous stress and heat flux, respectively. Therefore, the obtaining of higher-order of TNE quantities such as  $\Delta_3^*$  and  $\Delta_{4,2}^*$  could help us better understand the evolution of constitutive relationships.

In practical applications, if a same-order kinetic moment of  $f$  needs to be accurately known, it may be necessary to add the appropriate kinetic moment(s) of  $f^{(0)}$  to be preserved according to the dependency given by CE. For example, in DBM considering up to the second-order TNE effect, if we need further to accurately know  $\Delta_{5,3}^*$  or  $\mathbf{M}_{5,3}^*(f)$ , then according to Eq. (2.15), we need only to add  $\mathbf{M}_{6,4}^*(f^{(0)})$  to the list of kinetic moments to be preserved.

### 2.1.2. Discretization of the particle velocity space

The distribution function  $f$  in Boltzmann equation is defined in the phase space of particle position, particle velocity and time. In addition to discretizing space and time, it is also necessary to simultaneously discretize particle velocity space. Before discretization, we first assume that the non-equilibrium effects caused by the external force is sufficiently weak, so

the  $f$  in the external force term can be replaced by  $f^{eq}$  and Eq. (2.1) becomes,

$$\frac{\partial f}{\partial t} + \mathbf{v} \cdot \frac{\partial f}{\partial \mathbf{r}} + \mathbf{a} \cdot \frac{(\mathbf{u} - \mathbf{v})}{RT} f^{eq} = -\frac{1}{\tau} (f - f^{eq}). \quad (2.21)$$

After further discretizing the particle velocity space, Eq. (2.21) becomes,

$$\frac{\partial f_i}{\partial t} + \mathbf{v}_i \cdot \frac{\partial f_i}{\partial \mathbf{r}} + \mathbf{a} \cdot \frac{(\mathbf{u} - \mathbf{v}_i)}{RT} f_i^{eq} = -\frac{1}{\tau} (f_i - f_i^{eq}), \quad (2.22)$$

where  $f_i$  and  $f_i^{eq}$  are the discrete distribution function (DDF) and discrete equilibrium distribution function (DEDF), respectively.  $i = 1, \dots, N$ ,  $N$  is the number of discrete velocities. Unlike space and time discretization, the particle velocity can take any value range from  $(-\infty, +\infty)$ , which means the  $f_i$  and  $f_i^{eq}$  are not the exact distribution functions and do not have specific physical meaning. Here, what DBM gives are the most necessary physical constraints on the DDF and DEDF, that is, the kinetic moments preserved must keep their value unchanged before and after discretization. In other words, the integral form of kinetic moments preserved is equal to the summation form, as follows,

$$\int f \Psi(\mathbf{v}) d\mathbf{v} = \sum_i f_i \Psi(\mathbf{v}_i), \quad (2.23)$$

where  $\Psi(\mathbf{v}) = [1, \mathbf{v}, \mathbf{v}\mathbf{v}, \dots]$  represents the kinetic moments preserved. According to CE multi-scale analysis,  $f$  can be finally expressed by  $f^{eq}$  and Eq. (2.23) is equal to,

$$\int f^{eq} \Psi'(\mathbf{v}) d\mathbf{v} = \sum_i f_i^{eq} \Psi'(\mathbf{v}_i), \quad (2.24)$$

where  $\Psi'(\mathbf{v})$  represents the higher order kinetic moments.

The depth of TNE that DBM could describe varies according to the specific choice of kinetic moments. For example, the DBM considering the zero-order TNE effects requires five kinetic moments of  $f^{eq}$  ( $\mathbf{M}_0, \mathbf{M}_1, \mathbf{M}_{2,0}, \mathbf{M}_2, \mathbf{M}_{3,1}$ ). The DBM considering up to the first-order TNE effects requires seven kinetic moments of  $f^{eq}$  ( $\mathbf{M}_0, \mathbf{M}_1, \mathbf{M}_{2,0}, \mathbf{M}_2, \mathbf{M}_{3,1}, \mathbf{M}_3, \mathbf{M}_{4,2}$ ), and DBM considering up to the second-order TNE effects requires nine kinetic moments of  $f^{eq}$  ( $\mathbf{M}_0, \mathbf{M}_1, \mathbf{M}_{2,0}, \mathbf{M}_2, \mathbf{M}_{3,1}, \mathbf{M}_3, \mathbf{M}_{4,2}, \mathbf{M}_4, \mathbf{M}_{5,3}$ ). The details about the above kinetic moments are listed in Appendix A.

In this paper, as the first application of the new DBM model for magnetohydrodynamic flow, the first-order TNE effects are considered and analyzed, and the seven kinetic moments to be preserved could be written in matrix form as,

$$\mathbf{C} \cdot \mathbf{f}^{eq} = \hat{\mathbf{f}}^{eq}, \quad (2.25)$$

where  $\mathbf{C}$ ,  $\mathbf{f}^{eq}$ ,  $\hat{\mathbf{f}}^{eq}$  are the discrete velocity polynomial, discrete equilibrium distribution function and macroscopic quantities in matrix form, respectively. In order to determine the specific value of  $\mathbf{f}^{eq}$ , the discrete velocity model (DVM) needs to be constructed. The selection or construction of DVM is highly flexible, which is based on the comprehensive consideration of physical symmetry, stability and computational efficiency, etc.

### 2.1.3. Extraction and measurement of non-equilibrium effects

The most significant function of DBM beyond traditional hydrodynamic modelling is to extract and measure the non-equilibrium effects based on the non-conserved kinetic moments of  $(f - f^{eq})$ . At present, no matter the macroscopic or mesoscopic kinetic models, what are mainly concerned and used to describe the system are the physical quantities defined in hydrodynamic equations, such as density, temperature, pressure, viscosity and heat conduction. However, such physical quantities are insufficient to describe the system behaviors when the degree of non-continuity/non-equilibrium further increases.

By further investigating the kinetic moments, we find that for the first three conserved moments, the results obtained by integrating  $f^{eq}$  and  $f$  are the same. However, for the non-conserved moments, the results show difference, which constitutes the most basic description of the current TNE state. Based on non-conserved kinetic moments, more TNE information can be investigated such as the distribution of momentum and internal energy in different degrees of freedom, etc. Two kinds of TNE quantities have been defined by Eqs. (2.8)-(2.9). In this paper, the TNE quantities defined by four non-conserved kinetic moments are shown as follows,

$$\Delta_2^* = \sum_i (f_i - f_i^{eq}) \mathbf{v}_i^* \mathbf{v}_i^*, \quad (2.26)$$

$$\Delta_3^* = \sum_i (f_i - f_i^{eq}) \mathbf{v}_i^* \mathbf{v}_i^* \mathbf{v}_i^*, \quad (2.27)$$

$$\Delta_{3,1}^* = \frac{1}{2} \sum_i (f_i - f_i^{eq}) \left( \mathbf{v}_i^* \cdot \mathbf{v}_i^* + \eta_i^2 \right) \mathbf{v}_i^*, \quad (2.28)$$

$$\Delta_{4,2}^* = \frac{1}{2} \sum_i (f_i - f_i^{eq}) \left( \mathbf{v}_i^* \cdot \mathbf{v}_i^* + \eta_i^2 \right) \mathbf{v}_i^* \mathbf{v}_i^*. \quad (2.29)$$

Here, the  $\Delta_3^*$  can be regarded as the flux of NOMF, and the  $\Delta_{4,2}^*$  can be regarded as the flux of NOEF, respectively. The first role of  $\Delta_3^*$  and  $\Delta_{4,2}^*$  is to help understanding the evolution of stress and heat flux from a more fundamental level, and the second role is to help assessing the necessity of introducing second-order TNE effects in the constitutive relations of KMM (Xu & Zhang 2022; Zhang *et al.* 2022a).

It is obvious that *roughly equivalent physical function to DBM are the extended hydrodynamic equations obtained by KMM*. In addition to the conservation equations of mass, momentum and energy, the extended hydrodynamic equations also contain the evolution equations describing some higher order kinetic moments such as  $\mathbf{M}_3^*$  and  $\mathbf{M}_{4,2}^*$ . The first function of  $\Delta_{n+1}^*$  is to help understanding the evolution of  $\Delta_n^*$  from a more fundamental level, and the second function is to help assessing the necessity of introducing the  $(n+1)$ -th order TNE effects in the constitutive relations of KMM (Xu & Zhang 2022; Zhang *et al.* 2022a).

With the help of the phase space opened by each subcomponent of  $\Delta_{m,n}^*$ , the following non-equilibrium strength can be defined,

$$D_{m,n} = \left| \Delta_{m,n}^* \right|, \quad (2.30)$$

where the square of  $|\Delta_{m,n}^*|$  is equal to the sum of the squares of the individual components of  $\Delta_{m,n}^*$ . To give a rough description of the total TNE strength, the function in [Chen et al. \(2016\)](#) is also adopted, which is defined as,

$$D_T = \sqrt{|\Delta_2^*|^2 + |\Delta_{3,1}^*|^2 + |\Delta_3^*|^2 + |\Delta_{4,2}^*|^2}. \quad (2.31)$$

Further, the global averaged TNE strength  $\bar{D}_{m,n}$  and  $\bar{D}_T$  are defined as

$$\bar{D}_{m,n} = \frac{1}{N_x \times N_y} \sum D_{m,n}, \quad (2.32)$$

$$\bar{D}_T = \frac{1}{N_x \times N_y} \sum D_T, \quad (2.33)$$

where  $N_x$  and  $N_y$  are the grid numbers in  $x$  and  $y$  direction, respectively. Since any definition of TNE intensity depends on the research perspective, it is helpful to introduce TNE intensity vectors (each component is a non-equilibrium intensity of one perspective) to cross-locate the TNE intensity from multiple perspectives ([Xu et al. 2021d](#); [Zhang et al. 2022a](#)). Intuitive geometric correspondence is very helpful for grasping complex behaviors. Therefore, we can further open a phase space based on the components of the TNE intensity vector. Then the TNE intensity vector obtains an intuitive geometric correspondence.

*Entropy generation rate is an important concern in many fields related to compression science, such as shock wave physics, ICF and aerospace.* Conveniently, according to the non-equilibrium quantities defined before, the entropy production rate caused dissipation effects could be measured. The total entropy production rate is defined as ([Zhang et al. 2016, 2019b](#)),

$$\frac{dS_b}{dt} = \int \left( \Delta_{3,1}^* \cdot \nabla \frac{1}{T} - \frac{1}{T} \Delta_2^* : \nabla \mathbf{u} \right) dr, \quad (2.34)$$

where the entropy production rate can be divided by two parts, that is, the part denoted by NOMF and NOEF, respectively. The two parts are defined as,

$$\dot{S}_{NOMF} = \int -\frac{1}{T} \Delta_2^* : \nabla \mathbf{u} dr, \quad (2.35)$$

$$\dot{S}_{NOEF} = \int \Delta_{3,1}^* \cdot \nabla \frac{1}{T} dr. \quad (2.36)$$

## 2.2. Equations of electromagnetic field

The evolution of electromagnetic field is described by Maxwell equations,

$$\nabla \cdot \mathbf{E} = \frac{\rho}{\varepsilon_0}, \quad (2.37)$$

$$\nabla \times \mathbf{E} = -\frac{\partial \mathbf{B}}{\partial t}, \quad (2.38)$$

$$\nabla \cdot \mathbf{B} = 0, \quad (2.39)$$

$$\nabla \times \mathbf{B} = \mu_0 \mathbf{j} + \frac{1}{c^2} \frac{\partial \mathbf{B}}{\partial t}. \quad (2.40)$$

In this work, several assumptions are introduced to simplify the Maxwell equation as: (i) The Larmor radius of ion and electron are sufficiently small compared to the characteristic scale of the system, so the charge separation is ignored and the Poisson equation, that is, Eq. (2.37) degenerate, (ii) the displacement current is sufficiently small compared to the conduction current, so the second term on the right-hand side of Eq. (2.40) is ignored, (iii) the fluid is perfectly conductive and the electric conductivity is infinite, so the generalized Ohm's law is simplified as  $\mathbf{E} = -\mathbf{u} \times \mathbf{B}$ .

Physically, the divergence-free constraint Eq. (2.39) is always preserved if it is initially satisfied. However, the errors caused by long time numerical calculation can break this limit. To preserve the divergence-free constraint, the magnetic field  $\mathbf{B}$  is represented by the magnetic potential  $\mathbf{A}$  as  $\mathbf{B} = \nabla \times \mathbf{A}$ . For two-dimensional simulation,  $\mathbf{A}$  contains only one component  $A_z$ . The evolution of  $\mathbf{A}$  can be represented by the following equations,

$$\frac{\partial A_z}{\partial t} = -\mathbf{u} \cdot \nabla A_z = -u_x \frac{\partial A_z}{\partial x} - u_y \frac{\partial A_z}{\partial y}. \quad (2.41)$$

By solving Eq. (2.41), the divergence-free constraint will automatically hold during the numerical calculation. In order to construct MHD model, Eq. (2.22) and Eq. (2.41) needs to be combined. The method is to introduce the Lorentz force in the external force term (the third term on the left-hand side of Eq. (2.22)), and the acceleration  $\mathbf{a}$  is rewritten as  $\mathbf{a} = \mathbf{j} \times \mathbf{B} / \rho$ , where  $\mathbf{j} \times \mathbf{B}$  represent the Lorentz force as,

$$\mathbf{j} \times \mathbf{B} = \frac{\mathbf{B} \cdot \nabla \mathbf{B}}{\mu_0} - \nabla \left( \frac{B^2}{2\mu_0} \right), \quad (2.42)$$

where the first term is called the magnetic tension, while the second term is called the magnetic pressure, with which the total pressure is expressed as  $p^* = p + B^2/(2\mu_0)$ . Through CE analysis, it is easy to find that the first function of DBM is to recover the magnetohydrodynamic model described by the following equations,

$$\frac{\partial \rho}{\partial t} + \nabla \cdot (\rho \mathbf{u}) = 0, \quad (2.43)$$

$$\frac{\partial (\rho \mathbf{u})}{\partial t} + \nabla \cdot (\rho \mathbf{u} \mathbf{u} + p \mathbf{I}) = -\nabla \cdot \mathbf{P}' + \mathbf{j} \times \mathbf{B}, \quad (2.44)$$

$$\frac{\partial E_T}{\partial t} + \nabla \cdot [(E_T + p) \mathbf{u}] = \nabla \cdot (\kappa \nabla T + \mathbf{P}' \cdot \mathbf{u}) + (\mathbf{j} \times \mathbf{B}) \cdot \mathbf{u}. \quad (2.45)$$

where  $\mathbf{P}'$  is the viscous stress and  $\kappa$  is the heat conductivity.

In summary, the equations used for simulation are Eqs. (2.22), (2.41) and (2.42), and the schemes used for analyze the TNE are given by equations from (2.26) to (2.36). *As a model construction and TNE analysis method, what DBM presents are the basic constraints on the discrete formats.* The DBM itself does not give specific discrete formats. The specific discrete formats should be chosen according to the specific problem to be simulated.

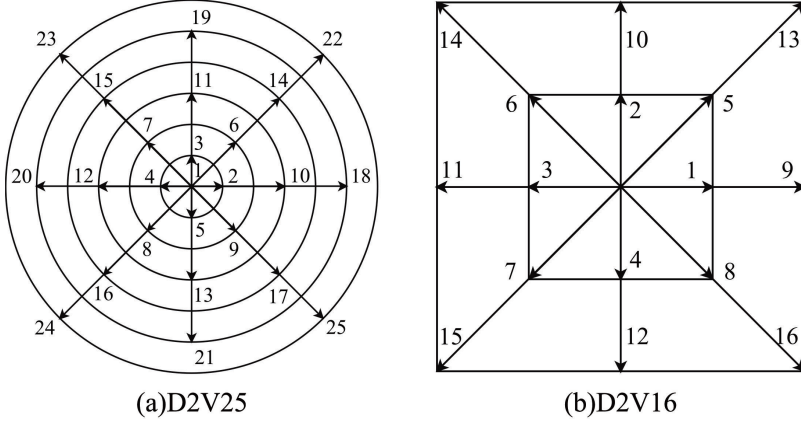


Figure 1: Schematics of two kinds of discrete velocity models used in the present paper. (a)D2V25, (b)D2V16. The numbers in the figures represent the index of discrete velocities.

### 3. Numerical Validation and Investigation

After the method formulation, a number of typical benchmark problems such as sod shock tube, thermal Couette flow and the compressible Orszag-Tang (OT) vortex problem are simulated, where the hydrodynamic behaviors are used to validate the plasma DBM. It should be noted that, all physical quantities used in the calculations are nondimensionalized, as shown in Appendix B.

In this paper, the first-order forward Euler finite difference scheme and the second-order non-oscillatory nonfree dissipative (NND) scheme are used to discrete spatial and temporary derivatives in Eq. (2.22) and Eq. (2.41), respectively. The second-order central difference scheme is used to discretize the space derivative in Eq. (2.42). Two two-dimensional DVMs are adopted in this paper. The DVM used to simulate the benchmark problems has 25 discrete velocities as shown in figure 1(a), and the DVM used to simulate the RMI has 16 discrete velocities as shown in figure 1(b).

The mathematical expressions of these two kinds of DVM are as follows,

$$\text{D2V25} : (v_{ix}, v_{iy}) = \begin{cases} 0, & i = 1 \\ c \left[ \cos \frac{(i-2)\pi}{2}, \sin \frac{(i-2)\pi}{2} \right], & i = 2 - 5, \\ 2c \left[ \cos \frac{(2i-3)\pi}{4}, \sin \frac{(2i-3)\pi}{4} \right], & i = 6 - 9, \\ 3c \left[ \cos \frac{(i-10)\pi}{2}, \sin \frac{(i-10)\pi}{2} \right], & i = 10 - 13, \\ 4c \left[ \cos \frac{(2i-11)\pi}{4}, \sin \frac{(2i-11)\pi}{4} \right], & i = 14 - 17, \\ 5c \left[ \cos \frac{(i-18)\pi}{2}, \sin \frac{(i-18)\pi}{2} \right], & i = 18 - 21, \\ 6c \left[ \cos \frac{(2i-19)\pi}{4}, \sin \frac{(2i-19)\pi}{4} \right], & i = 22 - 25, \end{cases} \quad (3.1)$$

$$\text{D2V16} : (v_{ix}, v_{iy}) = \begin{cases} \text{cyc} : c(\pm 1, 0), & 1 \leq i \leq 4, \\ c(\pm 1, \pm 1), & 1 \leq i \leq 8, \\ \text{cyc} : 2c(\pm 1, 0), & 9 \leq i \leq 12, \\ 2c(\pm 1, \pm 1), & 13 \leq i \leq 16, \end{cases} \quad (3.2)$$

where ‘cyc’ represents the indicates cyclic permutation.  $c$  is a free parameter to optimize the properties of the DVM.

In order to save space, here we only show the results of OT vortex problem. This problem is first proposed by Orszag and Tang in 1979 (Orszag & Tang 1979). Due to the complex vortex and shock wave structures generated during evolution, this problem has been widely used to demonstrate the validity of new models. Here, the initial configuration and conditions are identical to Jiang & Wu (1999), as follows,

$$\begin{aligned} \rho(x, y, 0) &= \gamma^2, & v_x(x, y, 0) &= -\sin y, \\ v_y(x, y, 0) &= \sin x, & p(x, y, 0) &= \gamma, \\ B_x(x, y, 0) &= -\sin y, & B_y(x, y, 0) &= \sin 2x, \end{aligned} \quad (3.3)$$

where  $\gamma$  is equal to  $5/3$ . The computational domain is  $[0, 2\pi] \times [0, 2\pi]$ , which has been divided into  $N_x \times N_y = 400 \times 400$  mesh-cells. The D2V25 model in figure 1 is used to discretize the velocity space, where  $c = 0.6$ ,  $\eta_0 = 0.4$  for  $i = 2, \dots, 5$ ,  $\eta_0 = 0.8$  for  $i = 6, \dots, 9$  and  $\eta_0 = 0$  for others. The time step is  $\Delta t = 5 \times 10^{-4}$ , the space step is  $\Delta x = \Delta y = 5 \times 10^{-3}\pi$ , the relaxation time is  $\tau = 1 \times 10^{-3}$ , and the number of extra degree of freedom is  $n = 1$ . Moreover, the periodic boundaries are applied in both  $x$  and  $y$  direction.

Figure 2 shows the results calculated by DBM. From figure 2(c), it is observed that the system is very complex, forming a variety of vortex and shock wave structures, especially in the center of the flow field. By comparing the DBM results in figures 2(a)-(c) with the MHD results in figures (12)-(14) given in Jiang & Wu (1999), it is found that the two sets of results are in good agreement. For quantitative comparison, the pressure distribution along  $y = 0.625\pi$  at time  $t = 3$  is extracted and plotted together with the result of Jiang & Wu (1999) in figure 2(d). It can be seen that the DBM results from  $x = 0.2$  to  $x = 0.4$  is slightly lower, while the rest of results is in good agreement with those of Jiang & Wu (1999), which proves the validity of the new magnetohydrodynamic DBM. In fact, the kinetics behavior of OT turbulence evolution is far from well studied. In addition to the comparison of the above HNE characteristics, the TNE characteristics are further extracted and plotted in figure 3.

Figure 3(a) shows the contour map of total TNE strength  $D_T$  at  $t = 3$ . It is found that the TNE effects are most pronounced in the shock front where high physical gradients exist. For the rest of the flows field, the TNE strength is weak, indicating that the system is close to the local thermodynamic equilibrium state. figure 3(b) shows the evolution of four kinds of entropy production rates with time. It can be seen that, both the four kinds of entropy production rates show two stages effect: before  $t = 1.7$ , the entropy production rates keep

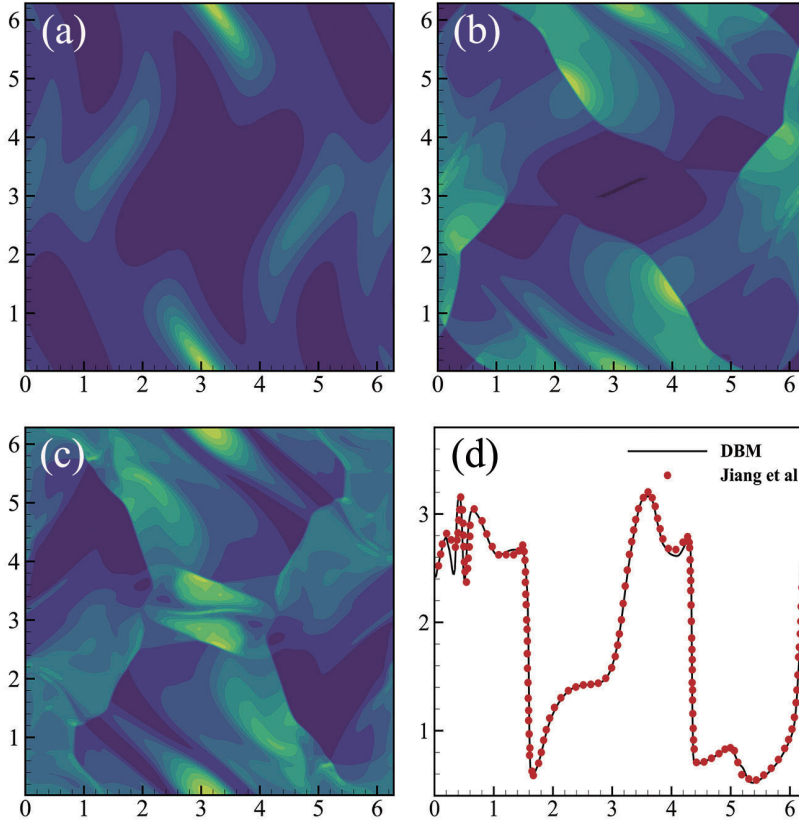


Figure 2: DBM results of Orszag-Tang vortex problem. (a) Pressure contour at time  $t = 0.5$  of DBM results. (b) Pressure contour at time  $t = 2$  of DBM results. (c) Pressure contour at time  $t = 3$  of DBM results. (d) Pressure distributions along  $y = 0.625\pi$  at  $t = 3$ . The solid line represent the DBM result while the red dots represent the result of [Jiang & Wu \(1999\)](#).

increasing with time; After  $t = 1.7$ , the entropy production rates reach the peak value and then keep decreasing with time. In fact, there is a positive correlation between the entropy production rate and the physical quantity gradient. Before  $t = 1.7$ , the evolution of flow field is in dominated and the velocity and temperature gradients keep increasing, which leads to the increase of entropy production rates. After  $t = 1.7$ , the dissipative effects are in dominated, resulting in the reduction of gradients and entropy production rates. Besides, in the early stage, it is found that the  $\dot{S}_{NOEF}$  increases from 0, while the  $\dot{S}_{NOMF}$  increases from about 0.1. This is because the initial temperature field is uniform and there exists no temperature gradient. For the initial velocity field, the initial velocity gradient induces a momentum exchange and leads to an initial entropy production rate  $\dot{S}_{NOMF}$ . Besides, as the flow field develops, the entropy production rate  $\dot{S}_{NOEF}$  exceeds  $\dot{S}_{NOMF}$  after  $t = 1$  and is always larger than  $\dot{S}_{NOMF}$  in the subsequent evolution, indicating that the entropy production caused by NOEF is in dominant in the late stage of OT vortex problem.

*From the perspective of compression science, generally, the increase of entropy production*

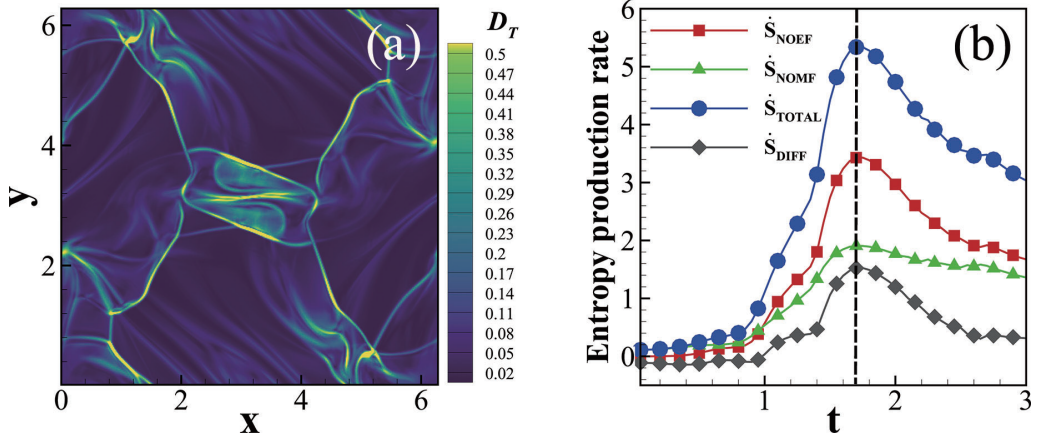


Figure 3: TNE effects of Orszag-Tang vortex problem. (a) Contour of total TNE strength  $D_T$  at  $t = 3$ , (b) evolution of three kinds of entropy production rate with time. The red line with square symbol corresponding to  $\dot{S}_{NOEF}$ . The green line with delta symbol corresponding to  $\dot{S}_{NOMF}$ . The blue line with circle symbol corresponding to the total entropy production rate. The gray line with diamond symbol corresponding to the difference between  $\dot{S}_{NOEF}$  and  $\dot{S}_{NOMF}$ .

rate predicts the increase of compression difficulty. In the process of OT evolution, the difficulty of compression is divided into stages: in the first stage, the difficulty of compression increases with time; in the second stage, the difficulty of compression decreases with time.

#### 4. Richtmyer-Meshkov instability

When the initial shock wave hits the perturbed interface, the non-collinear pressure and density gradient will induce vorticity at the perturbed interface and change the fluid velocity near the interface, resulting in the development of perturbation. In this section, the RMI induced by a shock wave passing through a heavy/light density interface is simulated by using the magnetohydrodynamic DBM. The effects of different initial magnetic field  $B_0$  on the evolution of RMI and the subsequent re-shock process, both the induced HNE and TNE effects, are carefully investigated.

This section consists of three subsections. In the first subsection, the initial configuration of RMI is given. In the next subsection, the HNE and TNE effects of RMI without magnetic field are investigated. In the last subsection, the HNE and TNE effects of RMI with different initial magnetic field are carefully investigated. Meanwhile, the entropy production rates under different initial magnetic field are calculated and analyzed. To ensure the resolution, a grid convergence analysis is performed and analyzed in Appendix C.

##### 4.1. Flow field

Figure 4 shows the initial flow field of RMI. The length and height of the two-dimension computation domain are 20 and 80, respectively. The computation domain is divided into

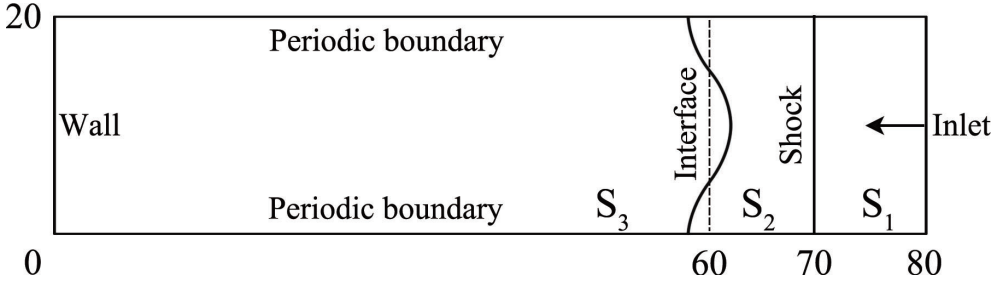


Figure 4: Schematic of initial configuration of Richtmyer-Meshkov instability.

$N_x \times N_y = 200 \times 800$  mesh-cells. Initially, a sinusoidal perturbation interface is located at  $y = 3N_y/4$ , with wavelength  $\lambda = d$ , where  $d = 20$  is equal to the length of computation domain. The amplitude is set to be  $y_0 = 0.1d$ , which corresponds to a small perturbation case. The initial shock wave is located at  $y = 7N_y/8$ , with the physical quantities on the left and right sides of the shock wave connected by the Rankine–Hugoniot conditions. Thus, the shock wave and perturbed interface separate the domain into three regions as  $S_1$ ,  $S_2$ , and  $S_3$ .  $S_1$  is the area that has been compressed by the passed shock wave.  $S_2$  is the region with high density and  $S_3$  is the region with light density. Furthermore, the periodic boundary conditions are applied to the boundaries in  $x$  direction, and the free inflow and solid boundary condition are applied to the boundaries at the top and bottom of  $y$  direction, respectively.

#### 4.2. RMI without magnetic field

In this section, the HNE and TNE effects of RMI without magnetic field are investigated. The initial hydrodynamic quantities are as follows,

$$\begin{cases} (\rho, u_x, u_y, p)_{S_1} = (3.1304, 0, -0.28005, 2.1187) \\ (\rho, u_x, u_y, p)_{S_2} = (2.3333, 0, 0, 1.4) \\ (\rho, u_x, u_y, p)_{S_3} = (1, 0, 0, 1.4) \end{cases} \quad (4.1)$$

With the above initial quantities, a shock wave with  $Ma = 1.2$  is formed to impact the sinusoidal perturbation interface. The Atwood number is  $At = 0.4$ . The D2V16 model in figure 1 is adopted to discrete the particle velocity space, and the parameters are  $c = 1$ ,  $\eta_0 = 5$  for  $i = 1, \dots, 4$  and  $\eta_0 = 0$  for others. The other parameters of DBM are as follows: space step  $\Delta x = \Delta y = 1 \times 10^{-1}$ , time step  $\Delta t = 1 \times 10^{-3}$ , relaxation time  $\tau = 1 \times 10^{-3}$  and the number of extra degrees of freedom  $n = 3$ , i.e., the specific heat ratio  $\gamma = 1.4$ .

##### 4.2.1. HNE characteristics

Figure 5 shows the density evolution in RMI via snapshots at times  $t = 0, 10, 15, 40, 70, 100, 250$ . At  $t = 10$ , the shock wave hits the interface and interacts with the interface. At  $t = 15$ , the shock wave passes through the interface, forming a reflected rarefaction wave propagating upward to top boundary and a transmission shock wave propagating downward to the bottom boundary. Meanwhile, the perturbation amplitude gradually decreases to zero with the motion of interface. Then, the interface reverses and the perturbation amplitude grows

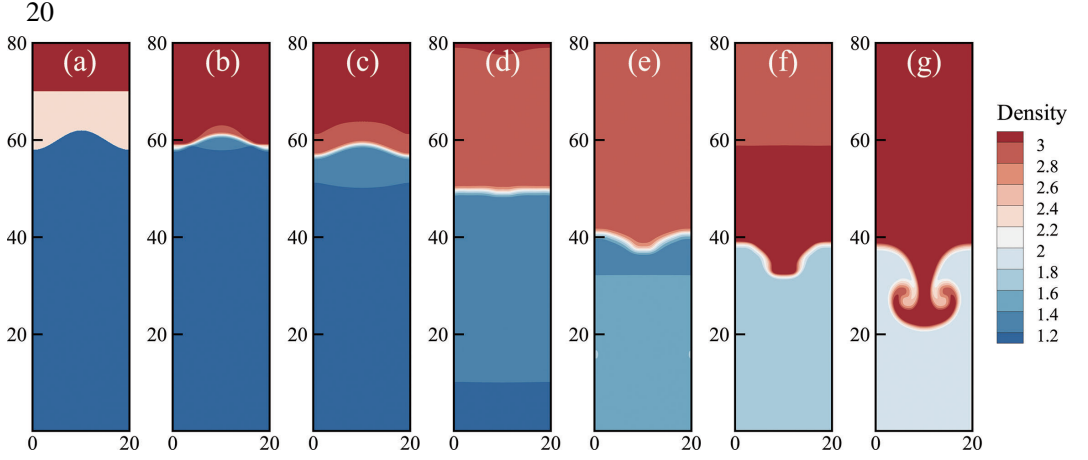


Figure 5: Density contours in the evolution of RMI without initial applied magnetic field at different times: (a)  $t = 0$ , (b)  $t = 10$ , (c)  $t = 15$ , (d)  $t = 40$ , (e)  $t = 70$ , (f)  $t = 100$ , (g)  $t = 250$ .

again, accompanied by the reversal of the initial perturbation interface peak and valley. At  $t = 40$ , the transmission shock wave moves to the bottom solid wall and reflects. At  $t = 70$ , the reflected transmission shock wave passes through the interface again, forming a reflected rarefaction wave to light fluids and a transmission shock wave to heavy fluids. Under the action of the secondary shock (reflected transmission shock wave), the speed of interface development is greatly accelerated and the speed difference on both sides of the interface increases rapidly. Then, the Kelvin-Helmholtz instability (KHI) appears at the head of the spike, eventually forming a mushroom-like structure. During the interface evolution, the light and heavy fluids continuously mix with each other.

#### 4.2.2. TNE effects

Figure 6(a) shows the global averaged TNE strength  $\bar{D}_T$ , NOMF  $\bar{D}_2$ , NOEF  $\bar{D}_{3,1}$ , the flux of NOMF  $\bar{D}_3$  and the flux of NOEF  $\bar{D}_{4,2}$  from  $t = 0$  to  $t = 500$ . It can be found that the strength of  $\bar{D}_2$  is much lower than other TNE effects, and the trend of  $\bar{D}_T$  is basically the same as that of  $\bar{D}_{3,1}$ , which means that the TNE effects of the whole system caused by viscosity are weaker than the TNE effects caused by heat conduction. The TNE strength  $\bar{D}_T$  of the system basically increases with time before about  $t = 320$ , while decreases with time after  $t = 320$ . In fact, there exists two competition mechanisms. Before  $t = 320$ , the evolution of RMI is located at linear and weak nonlinear development stage. With the development of the interface, the physical quantities gradient near the interface increases rapidly, and the non-equilibrium region augments, which cause the increasing of  $\bar{D}_T$ . After  $t = 320$ , the evolution of RMI is located at the late stage of nonlinear development. At this time, the dissipation effects such as viscosity and heat conduction are dominant, which increase the degree of mixing near the interface and reduce the gradient of physical quantities, causing the decrease of  $\bar{D}_T$ . Besides, from the red line ( $\bar{D}_T$ ), three key time points are marked, which are shown in the enlarged picture figure 6(b).

Figure 6(b) shows the the global averaged TNE strength  $\bar{D}_T$ , NOMF  $\bar{D}_2$ , NOEF  $\bar{D}_{3,1}$  and

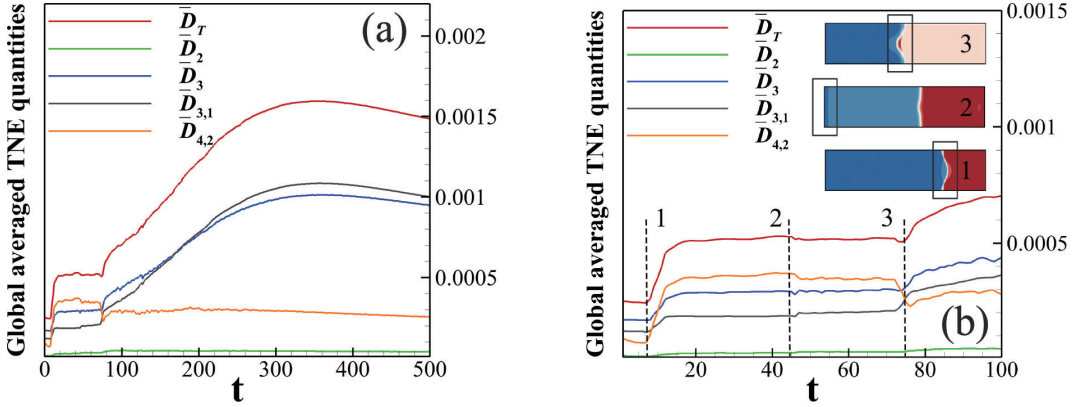


Figure 6: Contours of global averaged TNE quantities  $\bar{D}_T$ ,  $\bar{D}_2$ ,  $\bar{D}_3$ ,  $\bar{D}_{3,1}$  and  $\bar{D}_{4,2}$ . (a) The time ranges from  $t = 0$  to  $t = 500$ , (b) the time ranges from  $t = 0$  to  $t = 100$ .

the flux of NOEF  $\bar{D}_{4,2}$  from  $t = 0$  to  $t = 100$ . It is found that, before time point 1, TNE effects decrease very slowly with time due to dissipation effects. At time point 1, the shock wave passes through the interface, causing the distribution function near the interface to deviate greatly from the local thermodynamic equilibrium state. After time point 1, the dissipative effects tend to reduce TNE effects, while the high  $Kn$  makes it difficult to recover to the local thermodynamic equilibrium state, causing the increase of all TNE effects. At time point 2, the transmission shock wave hits the boundary and reflects. In this process, the gradients of macroscopic physical quantities change, resulting in the fluctuation of TNE quantities. At time point 3, the reflected transmission shock wave hits the interface again. Since the direction of the shock wave is opposite to that of the first time, not all TNE quantities increase. The flux of NOEF, i.e.,  $\bar{D}_{4,2}$  decreases, while the rest of the TNE quantities increase. Because the interface has reversed when the shock wave hits the interface for the second time, the vorticity generated is further deposited at the interface after time point 3, which leads to the accelerated development of the interface, the expansion of the non-equilibrium area and the continuous increase of all TNE quantities.

Figure 7 shows the contours of TNE quantities  $D_2$ ,  $D_3$ ,  $D_{3,1}$ ,  $D_{4,2}$  at  $t = 100$ , at which time the reflected transmission shock wave has passed the perturbed interface. From figure 7(a), it is found that  $D_2$  mainly distributed at shock wavefront and the perturbed interface, and the intensity at the shock wavefront is much higher than that at the perturbed interface. For the rest of the flow field, the  $D_2$  is almost zero. Therefore,  $D_2$  can be used to capture the location of shock wave during RMI. Due to the strong momentum transport and shear effects caused by the large density and velocity gradient, the  $D_2$  is most remarkable at shock wavefront. Figure 7(c) shows the distribution of  $D_{3,1}$ . It reaches the maximum value at perturbed interface. Thus,  $D_{3,1}$  can be used to capture the evolution of interface and the amplitude. In this case, the temperature gradient near perturbed interface is bigger than that near shock wavefront, causing strong energy transport. Thus, the  $D_{3,1}$  is most remarkable at perturbed interface. Though  $D_2$  and  $D_{3,1}$  can be used to identify the shock wavefront and

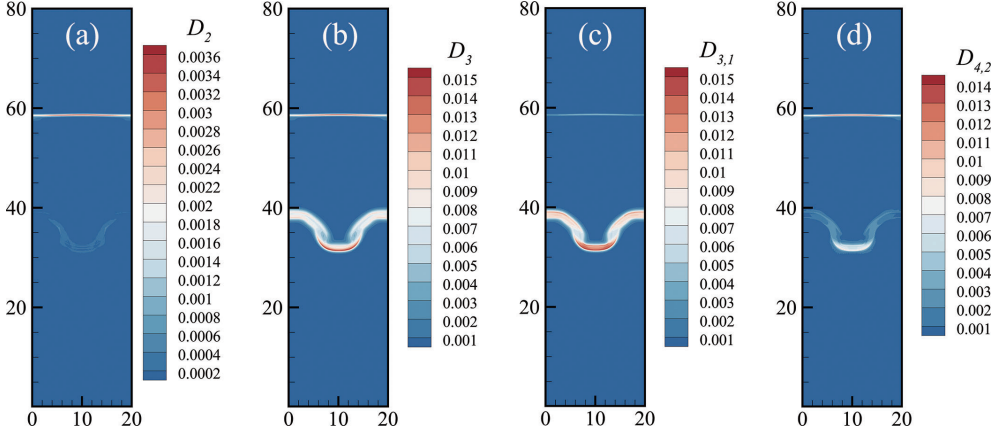


Figure 7: Contours of different TNE quantities of RMI at  $t = 100$ . (a) $D_2$ , (b) $D_3$ , (c) $D_{3,1}$ , (d) $D_{4,2}$

perturbed interface respectively, they cannot be used to identify both of them. Compared with  $D_2$  and  $D_{3,1}$ ,  $D_3$  and  $D_{4,2}$  are more suitable.  $D_3$  provides the most distinguishable interfaces, which is also proved by [Zhang \*et al.\* \(2019a\)](#). During the evolution of RMI, both of these four TNE quantities can be used as the supplement of the macroscopic quantities contours of flow field.

In order to investigate the evolution of non-equilibrium effects with time for a more detailed analysis, the axes  $x = N_x/2$  is selected and observed to see how the distribution of TNE quantities on the axes evolve over time. Figure 8(a) shows the distribution of the component  $\Delta_{2yy}^*$  of NOMF  $\Delta_2^*$ . It can be seen from the red line that  $\Delta_{2yy}^*$  mainly distributes in three areas marked with "1", "2", "3" from right to left, which exactly corresponding to rarefaction, material interface and transmission shock wave. Besides, the strength of  $\Delta_{2yy}^*$  near material interface is stronger than rarefaction but weaker than transmission shock wave. With time evolution, the intensity of  $\Delta_{2yy}^*$  near interface gradually decreases, but the intensity of  $\Delta_{2yy}^*$  near transmission shock wave gradually increases. Figure 8(b) shows the distribution of the component  $\Delta_{3,1y}^*$  of NOEF  $\Delta_{3,1}^*$ . It can be seen from the red line that the strength of  $\Delta_{3,1y}^*$  near material interface is much stronger than that near transmission shock wave. After the reflection of transmission shock wave, the direction of  $\Delta_{3,1y}^*$  reverses, which is different from  $\Delta_{2yy}^*$ . By further observing the distribution of  $\Delta_{3,1y}^*$  near material interface, it is found that the intensity of  $\Delta_{3,1y}^*$  first decreases then increases. The decreasing of  $\Delta_{3,1y}^*$  is mainly due to the increase of mixing area near interface, where the gradients of physical quantities decrease. The increasing of  $\Delta_{3,1y}^*$  is due to the passing of secondary shock, where the energy is transported from shock to material interface. Besides, there exists double-peak structure near material interface. In this case, the  $\Delta_{3,1y}^*$  first gets its maximum value at the right peak then the left one. The shift of the maximum peak depends on the direction of shock wave.

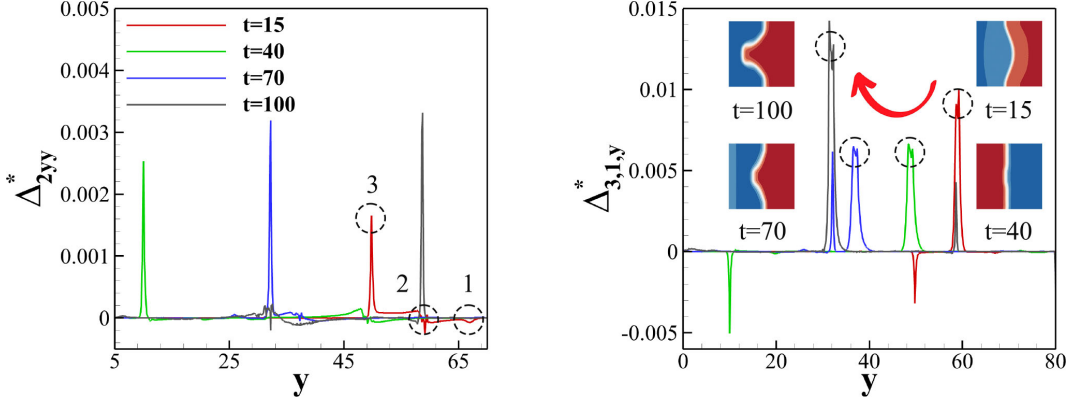


Figure 8: Distribution of different TNE quantities along  $N_x/2$  at  $t = 15$ ,  $t = 40$ ,  $t = 70$  and  $t = 100$ . (a)  $\Delta_{2yy}^*$ , (b)  $\Delta_{3,1y}^*$ .

Cases	$B_0$	Cases	$B_0$
Case I	0.01	Case VI	0.10
Case II	0.02	Case VII	0.15
Case III	0.03	Case VIII	0.20
Case IV	0.04	Case IX	0.25
Case V	0.05	Case X	0.30

Table 1: Settings for RMI with different initial applied magnetic fields.

### 4.3. RMI with magnetic field

The magnetic field can suppress the evolution of RMI through transporting the barochorically generated vorticity away from the interface (Samtaney 2003; Sano *et al.* 2013). In this section, the effects of magnetic fields on the evolution of RMI, including HNE and TNE effects, are analyzed. The initial magnetic field is set on the  $y$  direction, and the parameters setting in different cases are shown in Table 1.

#### 4.3.1. HNE characteristics

Figure 9 shows the density contours of different initial magnetic fields range from 0.01 to 0.30 at  $t = 250$ . It is found that the evolution of interface is gradually suppressed with the increase of magnetic fields. For the case of  $B_0 = 0.01$ , the Kelvin-Helmholtz instability (KHI) is still developed and observed, forming the "mushroom-like" structure. For the case of  $B_0 = 0.03$  and  $B_0 = 0.05$ , the KHI degenerates and the amplitude of interface decreases. From figures 9 (a)-(e), it can be observed that the interface can still reverse. However, from figure 9 (f), it is observed that the interface no longer reverses for the case  $B_0 = 0.30$ , indicating that there exists a critical magnetic field  $B_{0,C}$  under which the amplitude of interface can be suppressed to 0.

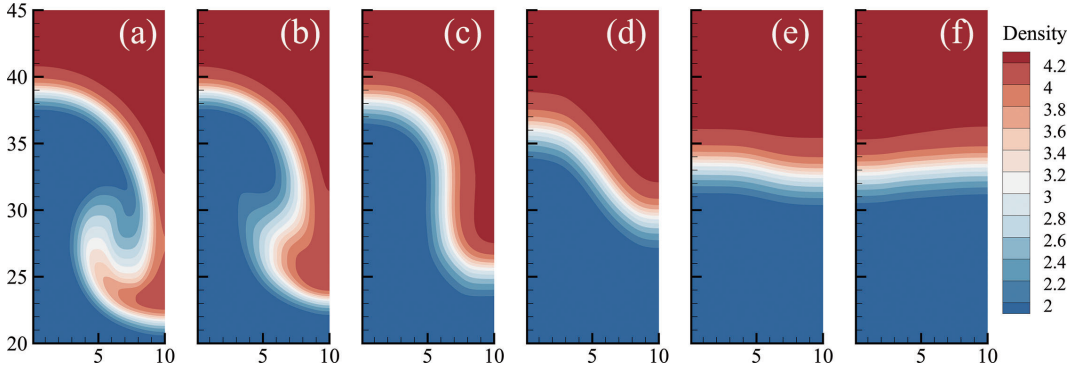


Figure 9: Density contours with different applied magnetic fields at  $t = 250$ . (a)  $B_0 = 0.01$ , (b)  $B_0 = 0.03$ , (c)  $B_0 = 0.05$ , (d)  $B_0 = 0.10$ , (e)  $B_0 = 0.20$ , (f)  $B_0 = 0.30$

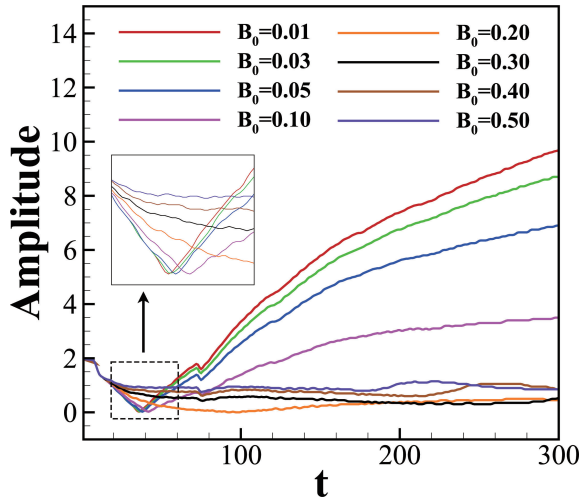


Figure 10: Evolution of amplitude of RMI with different initial applied magnetic fields from  $t = 0$  to  $t = 200$ .

Figure 10 further shows the evolution of interface amplitude with time under initial applied different magnetic fields. Obviously, the magnetic fields delay the time interface inverse. For the cases ( $B_0 \leq 0.05$ ), the magnetic fields have little effect on the flow field before inverse but can significantly inhibit the development of interface amplitude after inverse. With the increase of the magnetic fields, the influence of the secondary shock on the perturbation amplitude is weakened. This is mainly because the magnetic field inhibits the development of the interface, which reduces the perturbation amplitude when the secondary shock passing through interface. Thus, the induced vorticity reduces. With the increase of magnetic fields, a critical situation appears where the perturbation is nearly inhibited and the amplitude no longer increases. As the magnetic field further increase, the interface no longer reverse, and the vorticity induced by secondary shock will prevent the development of interface. When

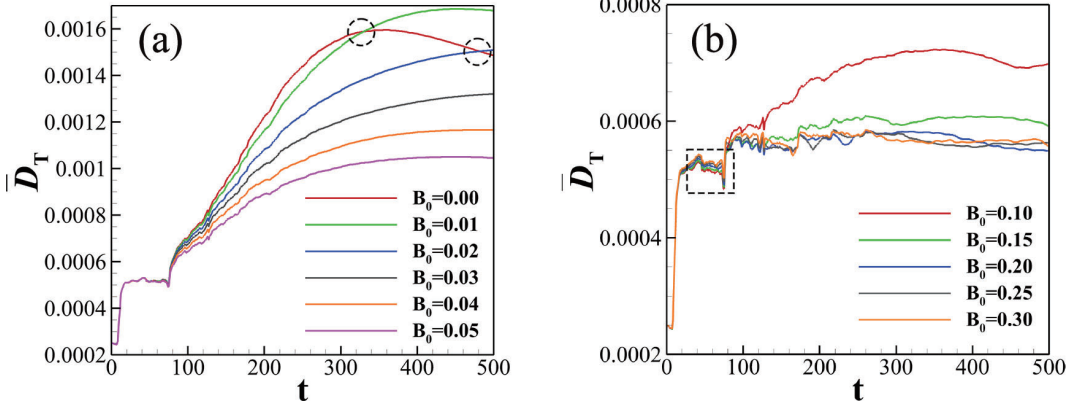


Figure 11: Evolution of global averaged TNE effects with different initial applied magnetic fields from  $t = 0$  to  $t = 500$ .

magnetic field exceeds the critical magnetic field, the stronger the magnetic field, the closer the interface shape is to the initial state.

#### 4.3.2. TNE effects

Figure 11(a) shows the global averaged TNE strength  $\bar{D}_T$  with different initial magnetic fields range from 0.00 to 0.05. It is observed that, before the secondary shock, the increase of magnetic fields shows little effect to  $\bar{D}_T$ . After secondary shock,  $\bar{D}_T$  quickly increases with the evolution of interface, and the magnetic fields show greatly effects for suppressing  $\bar{D}_T$ . However, it is found that  $\bar{D}_T$  for the case of  $B_0 = 0.01$  and  $B_0 = 0.02$  are greater than that of  $B_0 = 0.00$  after time marked with circle. This is because the magnetic fields suppress the shear effects around interface, thus delay the time KHI arises and decrease the strength of KHI. The emergence and development of KHI can enhance mixing and reduce the gradients of physical quantities, which is helpful for reducing  $\bar{D}_T$ . The inflection point of TNE intensity can be regarded as the criterion to judge whether KHI is fully developed. Before the inflection point, the development of perturbation amplitude dominates and the TNE is enhanced; after the inflection point, the fully development of KHI results in the enhancement of dissipation effect and the decrease of TNE intensity.

Figure 11(b) shows the global averaged TNE strength  $\bar{D}_T$  with different initial magnetic fields range from 0.10 to 0.30. It is found that the influence of magnetic field for TNE could be divided into two stages. Before the inverse of interface, as the strength of magnetic field increases, the TNE strength slightly increases. After the inverse of interface, the TNE strength decreases significantly with the increase of magnetic field strength. In fact, the magnetic field consistently inhibits the interface development during the RMI evolution. Before the interface inverse, the magnetic field inhibits the interface inverse, indirectly enhancing the physical quantity gradient near the interface, resulting in the enhancement of TNE intensity. After the interface inverse, the magnetic field inhibits the shear effect near the interface, as has been explained before. From figure 11(b), it can also be found that after secondary,  $\bar{D}_T$  keeps

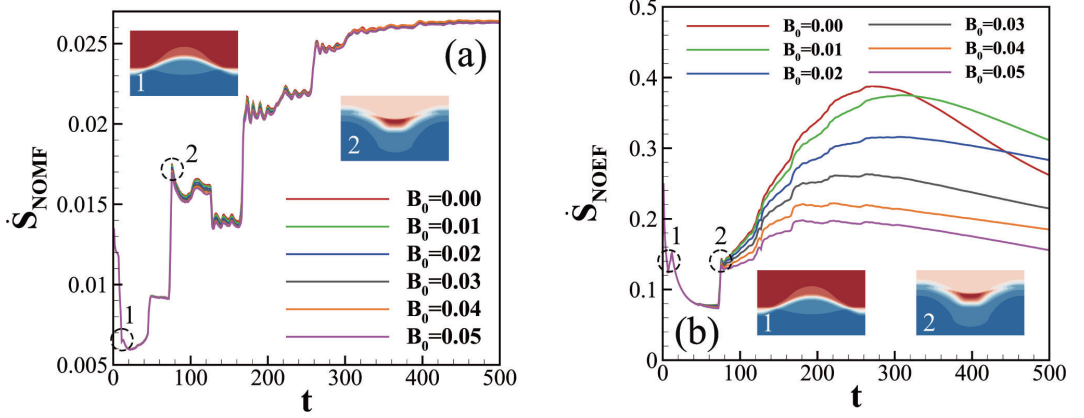


Figure 12: Evolution of entropy production rates from  $t = 0$  to  $t = 500$  with magnetic fields range from 0.01 to 0.05.

decreasing with the increase of magnetic fields, and there exists a critical magnetic field, above which  $\bar{D}_T$  no longer decreases. Thus, the magnetic field intensity  $B_{0,C}$ , corresponding to the minimum value  $\bar{D}_{T,min}$  of global averaged TNE intensity just after the reshock stage, can be used as the critical magnetic field intensity to inhibit the development of RMI interface.

#### 4.3.3. Entropy production

Figure 12 shows the two parts of entropy production rate  $\dot{S}_{NOMF}$  and  $\dot{S}_{NOEF}$  of the global system with magnetic fields range from 0.01 to 0.05. From figure 12(a) we can find that the entropy production rate  $\dot{S}_{NOMF}$  shows stages. Before the shock wave contact the perturbed interface, the rate sharply decreased. Then, after the shock wave contacts the solid wall and passed through interface again, the rate appears two jumps. After re-shock, the rate first decreases and then increases to the maximum. With the increase of magnetic fields, the values of  $\dot{S}_{NOMF}$  are basically the same. From figure 12(b), it is observed that when the shock first contacts the interface, the entropy production rate  $\dot{S}_{NOEF}$  suddenly increases, as shown by point '1', which is different from  $\dot{S}_{NOMF}$ . It means that the shock wave enhances physical quantity gradients near interface. When the transmitted shock wave passes interface again, as shown by point '2', the rate increases greatly, which is also observed from  $\dot{S}_{NOMF}$ . After re-shock, the rate first gradually increases and then decreases, which can be divided into two stages. When the initial magnetic field strength gradually increases, the  $\dot{S}_{NOEF}$  also shows no difference before re-shock, but is greatly reduced after re-shock. In general, the  $\dot{S}_{NOEF}$  contributes more to entropy increase than  $\dot{S}_{NOMF}$ , but the strength of  $\dot{S}_{NOEF}$  could be greatly inhibited by adding magnetic field.

Figure 13 shows the two parts of entropy production rate  $\dot{S}_{NOMF}$  and  $\dot{S}_{NOEF}$  of the global system with magnetic fields range from 0.10 to 0.30. From figure 12(a) and figure 13(a), it can be observed that the fluctuations in the  $\dot{S}_{NOMF}$  curve have been smoothed due to the increase of magnetic fields. Different from  $\dot{S}_{NOMF}$ , the evolution of  $\dot{S}_{NOEF}$  is strongly affected by magnetic fields. With the increase of magnetic fields, the evolution of  $\dot{S}_{NOEF}$

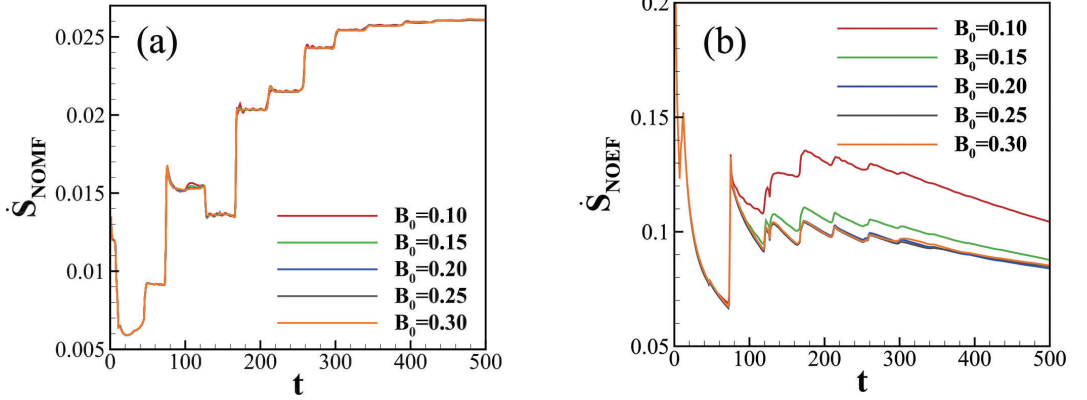


Figure 13: Evolution of entropy production rates from  $t = 0$  to  $t = 500$  with magnetic fields range from 0.10 to 0.30.

after re-shock is significantly inhibited. It can be observed that there exists a critical magnetic field, under which the  $\dot{S}_{NOEF}$  no longer decreases.

## 5. Conclusion and discussion

When the particle collision frequency is sufficiently high, the kinetic behaviors can be described by the reduced hydrodynamic equations. When the particle collision frequency is negligibly small, the kinetic behaviors can be described by the reduced Vlasov equation where the collision effect is completely ignored. The situation between the two extreme cases is generally difficult to treat with and consequently poorly understood, which is responsible for the fact that the kinetic effects caused by particle collision in ICF are still far from clear understanding although they have potential impact on ICF ignition.

To attack the problem, the preferred method/model needs to have simultaneously two physical functions. First, it can present numerical data which can recover the HNE and TNE behaviors we aim to investigate. Second, it can present methods which can be used to check the non-equilibrium state, describe and analyze the resulting effects. In the DBM, for the first physical function, the model equations are composed of a discrete Boltzmann equation coupled by a magnetic induction equation. For the second physical function, DBM intrinsically includes some schemes for studying the TNE behaviors. The most fundamental one is to use the non-conserved kinetic moments of  $(f - f^{eq})$  to check the TNE state and describe the TNE behaviors. The phase space description method based on the non-conserved kinetic moments of  $(f - f^{eq})$  presents an intuitive geometrical correspondence for the complicated TNE state and behaviors, which is important for the deep investigation and clear understanding. The first function is verified by recovering HNE behaviors of a number of typical benchmark problems including sod shock tube, thermal couette flow and OT vortex problem. Besides, the most relevant TNE behaviors of OT vortex problem are investigated for the first time. As a further application, the kinetic study on RMI system with

initial horizontal magnetic field is performed. Physical findings are as below: (i) Generally, the entropy production rate is in positive correlation to the difficulty of compression. During the evolution of OT system, the stage behavior of entropy production rate, first increases then decreases with time, shows the same stage behavior of compression difficulty. (ii) In the case without external magnetic field, the NOMF gets its maximum value near the shock front, while the NOEF gets its maximum value near the perturbed interface. During the perturbed interface inverse process of RMI, the NOEF along the central axis shows two-peak values near perturbed interface, and the impact of shock wave significantly enhances the NOEF. (iii) In the case with external magnetic field, the magnetic field shows inhibitory effects on the evolution of RMI. Specifically, the magnetic field has a pronounced inhibitory effect on the nonlinear stage, especially on the generation of KHI. Besides, there exists a critical magnetic field under which the amplitude of interface can be suppressed to 0. (iv) Before the interface inverse, the magnetic field indirectly enhances the TNE intensity by suppressing the interface inverse. After the interface inverse, the magnetic field significantly suppresses the TNE intensity by inhibiting the further development of the perturbed interface. (v) In terms of entropy production rate, the magnetic field has pronounced inhibitory effect on the entropy production rate caused by heat conduction, but has a weak effect on the entropy production rate caused by viscosity.

Potential applications of above physical findings are as follows: (i) Based on features of NOMF and NOEF, shock front and perturbed interface during RMI evolution can be physically captured in the numerical experiments. (ii) The magnetic field intensity  $B_{0,C}$ , corresponding to the minimum value  $\bar{D}_{T,min}$  of global averaged TNE intensity just after the re-shock stage, can be used as the critical magnetic field intensity to inhibit the development of RMI interface. (iii) From the perspective of entropy production rate, the magnetic field intensity  $B_{0,C}$ , corresponding to the minimum value of entropy production rate caused by heat conduction just after the re-shock stage, plays the same role. The future work includes two-fluid DBM where the ion and electrons are considered separately and Prantl number adjustable plasma DBM, etc.

**Acknowledgements.** The authors sincerely thank Lingxiao Li for his helpful suggestion on choosing discrete format. The authors thank Yudong Zhang, Chuandong Lin, Ge Zhang, Dejie Zhang, Yiming Shan, Jie Chen, Hanwei Li and Yingqi Jia for the helpful discussion on DBM. The authors thank Song Bai, Fuwen Liang, Feng Tian, Zihao He, Mingqing Nie, Zhengxi Zhu for the helpful discussion on results analysis.

**Funding.** This work was supported by the National Natural Science Foundation of China (grant numbers 52202460, 12172061 and 11975053), the National Key R D Program of China (grant numbers 2020YFC2201100, 2021YFC2202804, 2022YFB3403504), the Natural Science Foundation of Shandong Province (grant numbers ZR2020MA061), Shandong Province Higher Educational Youth Innovation Science and Technology Program (grant numbers 2019KJJ009), the opening project of State Key Laboratory of Explosion Science and Technology (Beijing Institute of Technology) (grant numbers KFJJ2023-02M), Foundation of Laboratory for Shock Wave and Detonation Physics.

**Declaration of interests.** The authors report no conflict of interest.

**Author ORCIDs.** Jiahui Song, <https://orcid.org/0000-0002-4996-6178>; Aiguo Xu, <https://orcid.org/0000-0002-6179-5973>; Long Miao, <https://orcid.org/0000-0001-5923-8740>; Feng Chen, <https://orcid.org/0000-0003-0094-2279>;

## Appendix A. Kinetic moments used to characterize the first-order and second-order TNE effects

Here, the kinetic moments used to characterize the first-order and second-order TNE effects are given as below,

$$M_0^{eq} = \sum_i f_i^{eq} = \rho, \quad (\text{A } 1)$$

$$M_{1,x}^{eq} = \sum_i f_i^{eq} v_{ix} = \rho u_x, \quad (\text{A } 2)$$

$$M_{1,y}^{eq} = \sum_i f_i^{eq} v_{iy} = \rho u_y, \quad (\text{A } 3)$$

$$M_{2,0}^{eq} = \sum_i f_i^{eq} \left( v_{ix}^2 + v_{iy}^2 + \eta_i^2 \right) = \rho \left[ (n+2) RT + u_x^2 + u_y^2 \right], \quad (\text{A } 4)$$

$$M_{2,xy}^{eq} = \sum_i f_i^{eq} v_{ix} v_{iy} = \rho u_x u_y, \quad (\text{A } 5)$$

$$M_{2,xx}^{eq} = \sum_i f_i^{eq} v_{ix} v_{ix} = \rho \left( RT + u_x^2 \right), \quad (\text{A } 6)$$

$$M_{2,yy}^{eq} = \sum_i f_i^{eq} v_{iy} v_{iy} = \rho \left( RT + u_y^2 \right), \quad (\text{A } 7)$$

$$M_{3,1,x}^{eq} = \sum_i f_i^{eq} \left( v_{ix}^2 + v_{iy}^2 + \eta_i^2 \right) v_{ix} = \rho u_x \left[ (n+4) RT + u_x^2 + u_y^2 \right], \quad (\text{A } 8)$$

$$M_{3,1,y}^{eq} = \sum_i f_i^{eq} \left( v_{ix}^2 + v_{iy}^2 + \eta_i^2 \right) v_{iy} = \rho u_y \left[ (n+4) RT + u_x^2 + u_y^2 \right], \quad (\text{A } 9)$$

$$M_{3,xxx}^{eq} = \sum_i f_i^{eq} v_{ix}^3 = \rho u_x \left( 3RT + u_x^2 \right), \quad (\text{A } 10)$$

$$M_{3,yyy}^{eq} = \sum_i f_i^{eq} v_{iy}^3 = \rho u_y \left( 3RT + u_y^2 \right), \quad (\text{A } 11)$$

$$M_{3,xyx}^{eq} = \sum_i f_i^{eq} v_{ix}^2 v_{iy} = \rho u_y \left( RT + u_x^2 \right), \quad (\text{A } 12)$$

$$M_{3,xyy}^{eq} = \sum_i f_i^{eq} v_{ix} v_{iy}^2 = \rho u_x \left( RT + u_y^2 \right), \quad (\text{A } 13)$$

$$\begin{aligned}
M_{4,2,xx}^{eq} &= \sum_i f_i^{eq} \left( v_{ix}^2 + v_{iy}^2 + \eta_i^2 \right) v_{ix}^2 \\
&= \rho \left[ (n+4)R^2T^2 + RT \left( (n+7)u_x^2 + u_y^2 \right) + u_x^2 \left( u_x^2 + u_y^2 \right) \right], \quad (A 14)
\end{aligned}$$

$$\begin{aligned}
M_{4,2,yy}^{eq} &= \sum_i f_i^{eq} \left( v_{ix}^2 + v_{iy}^2 + \eta_i^2 \right) v_{iy}^2 \\
&= \rho \left[ (n+4)R^2T^2 + RT \left( (n+7)u_y^2 + u_x^2 \right) + u_y^2 \left( u_x^2 + u_y^2 \right) \right], \quad (A 15)
\end{aligned}$$

$$M_{4,2,xy}^{eq} = \sum_i f_i^{eq} \left( v_{ix}^2 + v_{iy}^2 + \eta_i^2 \right) v_{ix}v_{iy} = \rho u_x u_y \left[ (n+6)RT + u_x^2 + u_y^2 \right], \quad (A 16)$$

$$M_{4,xxxx}^{eq} = \sum_i f_i^{eq} v_{ix}^4 = \rho \left( 3R^2T^2 + 6RTu_x^2 + u_x^4 \right), \quad (A 17)$$

$$M_{4,yyyy}^{eq} = \sum_i f_i^{eq} v_{iy}^4 = \rho \left( 3R^2T^2 + 6RTu_y^2 + u_y^4 \right), \quad (A 18)$$

$$M_{4,xxxy}^{eq} = \sum_i f_i^{eq} v_{ix}^3 v_{iy} = \rho u_x u_y \left( 3RT + u_x^2 \right), \quad (A 19)$$

$$M_{4,xyyy}^{eq} = \sum_i f_i^{eq} v_{ix} v_{iy}^3 = \rho u_x u_y \left( 3RT + u_y^2 \right), \quad (A 20)$$

$$M_{4,xxyy}^{eq} = \sum_i f_i^{eq} v_{ix}^2 v_{iy}^2 = \rho \left( RT + u_x^2 \right) \left( RT + u_y^2 \right), \quad (A 21)$$

$$\begin{aligned}
M_{5,3,xxx}^{eq} &= \sum_i f_i^{eq} \left( v_{ix}^2 + v_{iy}^2 + \eta_i^2 \right) v_{ix}^3 \\
&= \rho u_x \left[ 3(n+6)R^2T^2 + RT \left( (n+11)u_x^2 + 3u_y^2 \right) + u_x^2 \left( u_x^2 + u_y^2 \right) \right], \quad (A 22)
\end{aligned}$$

$$\begin{aligned}
M_{5,3,yyy}^{eq} &= \sum_i f_i^{eq} \left( v_{ix}^2 + v_{iy}^2 + \eta_i^2 \right) v_{iy}^3 \\
&= \rho u_y \left[ 3(n+6)R^2T^2 + RT \left( (n+11)u_y^2 + 3u_x^2 \right) + u_y^2 \left( u_x^2 + u_y^2 \right) \right], \quad (A 23)
\end{aligned}$$

$$\begin{aligned}
M_{5,3,xyy}^{eq} &= \sum_i f_i^{eq} \left( v_{ix}^2 + v_{iy}^2 + \eta_i^2 \right) v_{ix}^2 v_{iy} \\
&= \rho u_y \left[ (n+6)R^2T^2 + RT \left( (n+9)u_x^2 + u_y^2 \right) + u_x^2 \left( u_x^2 + u_y^2 \right) \right], \quad (A 24)
\end{aligned}$$

$$\begin{aligned}
M_{5,3,xyy}^{eq} &= \sum_i f_i^{eq} \left( v_{ix}^2 + v_{iy}^2 + \eta_i^2 \right) v_{ix} v_{iy}^2 \\
&= \rho u_x \left[ (n+6)R^2T^2 + RT \left( (n+9)u_y^2 + u_x^2 \right) + u_y^2 \left( u_x^2 + u_y^2 \right) \right], \quad (\text{A } 25)
\end{aligned}$$

where  $p = \rho RT$  obeys the ideal gas law.

## Appendix B. Non-dimensional quantities

All of the physical quantities used in this paper are dimensionless according to the following equations,

$$\hat{\rho} = \frac{\rho}{\rho_0}, \hat{T} = \frac{T}{T_0}, \hat{P} = \frac{P}{\rho_0 R T_0}, (\hat{t}, \hat{\tau}) = \frac{(t, \tau)}{\sqrt{R T_0}}, \hat{r}_\alpha = \frac{r_\alpha}{L_0}, \quad (\text{B } 1)$$

$$(\hat{v}_\alpha, \hat{c}_\alpha, \hat{u}_\alpha) = \frac{(v_\alpha, c_\alpha, u_\alpha)}{(L_0/t_0)}, \hat{B} = \frac{B L_0}{t_0} \sqrt{\mu_0 \rho_0}, \quad (\text{B } 2)$$

$$\hat{\kappa} = \frac{\kappa}{\rho_0 R L_0 \sqrt{R T_0}}, \hat{\mu} = \frac{\mu}{\rho_0 L_0 \sqrt{R T_0}}, \quad (\text{B } 3)$$

where subscript ‘0’ represents the reference physical quantities.

## Appendix C. Grid convergence test

In order to verify the effectiveness of numerical resolution, a grid convergence test is performed. Four kinds of grid numbers are selected as  $N_x \times N_y = 50 \times 200$ ,  $N_x \times N_y = 100 \times 400$ ,  $N_x \times N_y = 200 \times 800$  and  $N_x \times N_y = 400 \times 1600$ . The corresponding space steps are  $\Delta x = \Delta y = 4 \times 10^{-1}$ ,  $\Delta x = \Delta y = 2 \times 10^{-1}$ ,  $\Delta x = \Delta y = 1 \times 10^{-1}$ ,  $\Delta x = \Delta y = 5 \times 10^{-2}$ , respectively. The other calculation parameter settings of DBM are: time step  $\Delta t = 1 \times 10^{-1}$ , relaxation time  $\tau = 1 \times 10^{-3}$  and the number of extra degrees of freedom  $n = 3$ , i.e., the specific heat ratio  $\gamma = 1.4$ . Figure 14 shows the distribution of density and temperature along  $y = 20$ . It can be seen that the results of  $200 \times 800$  and  $400 \times 1600$  meshes are quite identical. By comprehensively considering numerical resolution and computational cost, the  $200 \times 800$  meshed are selected for calculation and analysis in this paper.

## REFERENCES

- ABU-SHAWAREB, H, ACREE, R, ADAMS, P, ADAMS, J, ADDIS, B, ADEN, R, ADRIAN, P, AFEYAN, BB, AGGLETON, M, AGHAIAN, L & OTHERS 2022 Lawson criterion for ignition exceeded in an inertial fusion experiment. *Physical Review Letters* **129** (7), 075001.
- ARNETT, DAVID 2000 The role of mixing in astrophysics. *The Astrophysical Journal Supplement Series* **127** (2), 213.
- ASAHINA, T, NAGATOMO, H, SUNAHARA, A, JOHZAKI, T, HATA, M, MIMA, K & SENTOKU, Y 2017 Validation of thermal conductivity in magnetized plasmas using particle-in-cell simulations. *Physics of Plasmas* **24** (4), 042117.

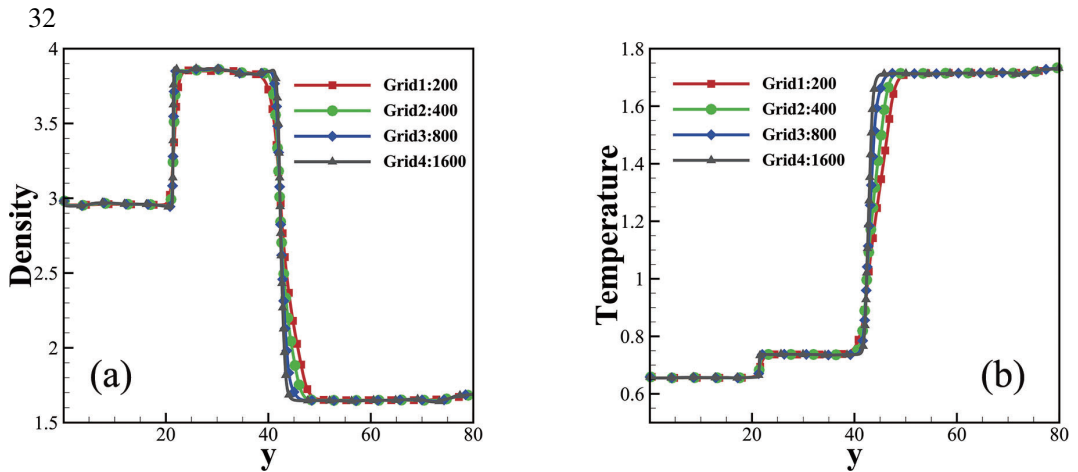


Figure 14: Distribution of physical quantities along  $x = 10$  of four kinds of grid at  $t = 100$ .  
(a)Density, (b)Temperature.

- BAKHSH, ABEER 2022 Linear analysis of magnetohydrodynamic richtmyer–meshkov instability in cylindrical geometry for double interfaces in the presence of an azimuthal magnetic field. *Physics of Fluids* **34** (11), 114120.
- BAO, YUE, QIU, RUOFAN, ZHOU, KANG, ZHOU, TAO, WENG, YUXIN, LIN, KAI & YOU, YANCHENG 2022 *Physics of Fluids* **34**, 046109.
- BETTI, R & HURRICANE, OA 2016 Inertial-confinement fusion with lasers. *Nature Physics* **12** (5), 435–448.
- BHATNAGAR, PRABHU LAL, GROSS, EUGENE P & KROOK, MAX 1954 *Physical Review* **94**, 511.
- BIRD, GA 1998 *Computers & Mathematics with Applications* **35**, 1–14.
- BOND, D, WHEATLEY, V, SAMTANEY, RAVI & PULLIN, DI 2017a *Journal of Fluid Mechanics* **833**, 332–363.
- BOND, D, WHEATLEY, V, SAMTANEY, RAVI & PULLIN, DI 2017b Richtmyer–meshkov instability of a thermal interface in a two-fluid plasma. *Journal of Fluid Mechanics* **833**, 332–363.
- BROUILLETTE, MARTIN 2002 The richtmyer–meshkov instability. *Annual Review of Fluid Mechanics* **34** (1), 445–468.
- CAI, HONG-BO, YAN, XIN-XIN, YAO, PEI-LIN & ZHU, SHAO-PING 2021 Hybrid fluid–particle modeling of shock-driven hydrodynamic instabilities in a plasma. *Matter and Radiation at Extremes* **6** (3), 035901.
- CAI, H. B., ZHANG, W. S., DU, B., YAN, X. X., SHAN, L. Q., HAO, L., LI, Z. C., ZHANG, F., GONG, T., YANG, D., ZOU, S. Y., ZHU, S. P. & HE, X. T. 2020 *High Power Laser and Particle Beams* **32**, 092007.
- CAO, JINTAO, WU, ZHENGWEI, REN, HAIJUN & LI, DING 2005 *Physics of Plasmas* **15**, 042102.
- CHEN, FENG, XU, AIGUO & ZHANG, GUANGCAI 2018a *Physics of Fluids* **30**, 102105.
- CHEN, FENG, XU, AIGUO, ZHANG, YUDONG, GAN, YANBIAO, LIU, BINGBING & WANG, SHUANG 2022a *Frontiers of Physics* **17**, 1–13.
- CHEN, FENG, XU, AIGUO, ZHANG, YUDONG & ZENG, QINGKAI 2020 *Physics of Fluids* **32**, 104111.
- CHEN, FENG, XU, AI-GUO & ZHANG, GUANG-CAI 2016 *Frontiers of Physics* **11**, 1–14.
- CHEN, JIE, XU, AIGUO, CHEN, DAWEI, ZHANG, YUDONG & CHEN, ZHIHUA 2022b *Physical Review E* **106**, 015102.
- CHEN, SHIYI, CHEN, HUDONG, MARTNEZ, DANIEL & MATTHAEUS, WILLIAM 1991 *Physical Review Letters* **67**, 3776.
- CHEN, W. F. & ZHAO, W.W. 2017 *Moment equations and numerical methods for rarefied gas flows (in Chinese)*, 1st edn. Science Press, Beijing.

- CHEN, Z, SHU, C & TAN, D 2018*b* *Physics of Fluids* **30**, 103605.
- CZELUSNIAK, LUIZ EDUARDO, MAPELLI, VINÍCIUS PESSOA, WAGNER, ALEXANDER J & CABEZAS-GÓMEZ, LUBEN 2022 Shaping the equation of state to improve numerical accuracy and stability of the pseudopotential lattice boltzmann method. *Physical Review E* **105** (1), 015303.
- DE ROSIS, ALESSANDRO, AL-ADHAM, JOANNE, AL-ALI, HAMDA & MENG, RAN 2021*a* *Physics of Fluids* **33**, 035143.
- DE ROSIS, ALESSANDRO, LIU, RUIZHI & REVELL, ALISTAIR 2021*b* *Physics of Fluids* **8**, 085114.
- DELLAR, PAUL J 2002 *Journal of Computational Physics* **179**, 95–126.
- GAN, YANBIAO, XU, AIGUO, LAI, HUILIN, LI, WEI, SUN, GUANGLAN & SUCCI, SAURO 2022 Discrete boltzmann multi-scale modelling of non-equilibrium multiphase flows. *Journal of Fluid Mechanics* **951**, A8.
- GAN, YANBIAO, XU, AIGUO, ZHANG, GUANGCAI & YANG, YANG 2013 Lattice bgk kinetic model for high-speed compressible flows: Hydrodynamic and nonequilibrium behaviors. *EPL (Europhysics Letters)* **103** (2), 24003.
- GAN, YANBIAO, XU, AIGUO, ZHANG, GUANGCAI, ZHANG, YUDONG & SUCCI, SAURO 2018 Discrete boltzmann trans-scale modeling of high-speed compressible flows. *Physical Review E* **97** (5), 053312.
- HUANG, QIUXIANG, TIAN, FANG-BAO, YOUNG, JOHN & LAI, JOSEPH CS 2021 Transition to chaos in a two-sided collapsible channel flow. *Journal of Fluid Mechanics* **926**, A15.
- JI, JEONG-YOUNG & HELD, ERIC D 2013 Closure and transport theory for high-collisionality electron-ion plasmas. *Physics of Plasmas* **20** (4), 042114.
- JIANG, GUANG-SHAN & WU, CHENG-CHIN 1999 *Journal of Computational Physics* **150**, 561–594.
- KEENAN, BRETT D, SIMAKOV, ANDREI N, CHACÓN, LUIS & TAITANO, WILLIAM T 2017 *Physical Review E* **96**, 053203.
- KHOKHLOV, AM, ORAN, ES & THOMAS, GO 1999 Numerical simulation of deflagration-to-detonation transition: the role of shock–flame interactions in turbulent flames. *Combustion and flame* **117** (1-2), 323–339.
- KUMAR, GN SASHI & MAHESHWARI, NK 2020 Viscous multi-species lattice boltzmann solver for simulating shock-wave structure. *Computers & Fluids* **203**, 104539.
- LAI, HUILIN, XU, AIGUO, ZHANG, GUANGCAI, GAN, YANBIAO, YING, YANGJUN & SUCCI, SAURO 2016 *Physical Review E* **94**, 023106.
- LARROCHE, O, RINDERKNECHT, HG, ROSENBERG, MJ, HOFFMAN, NM, ATZENI, S, PETRASSO, RD, AMENDT, PA & SÉGUIN, FH 2016 Ion-kinetic simulations of d-3he gas-filled inertial confinement fusion target implosions with moderate to large knudsen number. *Physics of Plasmas* **23** (1), 012701.
- LEDESMA-AGUILAR, RODRIGO, VELLA, DOMINIC & YEOMANS, JULIA M 2014 Lattice-boltzmann simulations of droplet evaporation. *Soft Matter* **10** (41), 8267–8275.
- LEI, FAN, DING, JUCHUN, SI, TING, ZHAI, ZHIGANG & LUO, XISHENG 2017 Experimental study on a sinusoidal air/sf interface accelerated by a cylindrically converging shock. *Journal of Fluid Mechanics* **826**, 819–829.
- LI, HANWEL, XU, AIGUO, ZHANG, GE & SHAN, YIMING 2022*a* Rayleigh–taylor instability under multi-mode perturbation: Discrete boltzmann modeling with tracers. *Communications in Theoretical Physics* **74** (11), 115601.
- LI, QING, LUO, KH, GAO, YJ & HE, YL 2012 *Physical Review E* **85**, 026704.
- LI, QING, LUO, KAI HONG, KANG, QJ, HE, YL, CHEN, Q & LIU, Q 2016 Lattice boltzmann methods for multiphase flow and phase-change heat transfer. *Progress in Energy and Combustion Science* **52**, 62–105.
- LI, YUAN, BAKHSH, ABEER & SAMTANEY, RAVI 2022*b* Linear stability of an impulsively accelerated density interface in an ideal two-fluid plasma. *Physics of Fluids* **34** (3), 036103.

- LI, YAOFENG, LAI, HUILIN, LIN, CHUANDONG & LI, DEMEI 2022c Influence of the tangential velocity on the compressible kelvin-helmholtz instability with nonequilibrium effects. *Frontiers of Physics* **17** (6), 1–17.
- LI, ZHI-HUI, PENG, AO-PING, ZHANG, HAN-XIN & YANG, JAW-YEN 2015 *Progress in Aerospace Sciences* **74**, 81–113.
- LIN, CHUANDONG & LUO, KAI H 2019 Discrete boltzmann modeling of unsteady reactive flows with nonequilibrium effects. *Physical Review E* **99** (1), 012142.
- LIN, CHUANDONG, LUO, KAI H, XU, AIGUO, GAN, YANBIAO & LAI, HUILIN 2021 *Physical Review E* **103**, 013305.
- LIN, CHUANDONG, XU, AIGUO, ZHANG, GUANGCAI, LUO, KAI HONG & LI, YINGJUN 2017 *Physical Review E* **96**, 053305.
- LIU, CHANG & XU, KUN 2017 A unified gas kinetic scheme for continuum and rarefied flows v: multiscale and multi-component plasma transport. *Communications in Computational Physics* **22** (5), 1175–1223.
- LIU, HAO-CHEN, YU, BIN, CHEN, HAO, ZHANG, BIN, XU, HUI & LIU, HONG 2020 Contribution of viscosity to the circulation deposition in the richtmyer–meshkov instability. *Journal of Fluid Mechanics* **895**, A10.
- LIU, ZHIPENG, SONG, JIAHUI, XU, AIGUO, ZHANG, YUDONG & XIE, KAN 2022 *Proceedings of the Institution of Mechanical Engineers, Part C: Journal of Mechanical Engineering Science* p. 09544062221075943.
- MCMULLEN, RYAN M, KRYGIER, MICHAEL C, TORCZYNSKI, JOHN R & GALLIS, MICHAEL A 2022 *Physical Review Letters* **128**, 114501.
- MENG, BAOQING, ZENG, JUNSHENG, TIAN, BAOLIN, ZHOU, RUI & SHEN, WEIDONG 2019 Modeling and simulation of a single-mode multiphase richtmyer–meshkov instability with a large stokes number. *AIP Advances* **9** (12), 125311.
- MESHKOV, \_E E 1969 Instability of the interface of two gases accelerated by a shock wave. *Fluid Dynamics* **4** (5), 101–104.
- MOSTERT, WOUTER, PULLIN, DALE I, WHEATLEY, VINCENT & SAMTANEY, RAVI 2017 Magnetohydrodynamic implosion symmetry and suppression of richtmyer–meshkov instability in an octahedrally symmetric field. *Physical Review Fluids* **2** (1), 013701.
- MOSTERT, WOUTER, WHEATLEY, VINCENT, SAMTANEY, RAVI & PULLIN, DALE I 2015 *Physics of Fluids* **27**, 104102.
- ORSZAG, STEVEN A & TANG, CHA-MEI 1979 Small-scale structure of two-dimensional magnetohydrodynamic turbulence. *Journal of Fluid Mechanics* **90** (1), 129–143.
- PATTISON, MJ, PREMNATH, KN, MORLEY, NB & ABDOU, MA 2008 *Fusion Engineering and Design* **83**, 557–572.
- QIN, JIANHUA & DONG, GUODAN 2021 The richtmyer–meshkov instability of concave circular arc density interfaces in hydrodynamics and magnetohydrodynamics. *Physics of Fluids* **33** (3), 034122.
- QIU, RUOFAN, BAO, YUE, ZHOU, TAO, CHE, HUANHUAN, CHEN, RONGQIAN & YOU, YANCHENG 2020 *Physics of Fluids* **32**, 106106.
- QIU, RUOFAN, ZHOU, TAO, BAO, YUE, ZHOU, KANG, CHE, HUANHUAN & YOU, YANCHENG 2021 *Physical Review E* **103**, 053113.
- QIU, ZHIYONG, WU, ZHENGWEI, CAO, JINTAO & LI, DING 2008 *Physics of Plasmas* **15**, 042305.
- RICHTMYER, ROBERT D. 1960 Taylor instability in shock acceleration of compressible fluids. *Communications on Pure and Applied Mathematics* pp. 297–319.
- RINDERKNECHT, HANS G, AMENDT, PA, WILKS, SC & COLLINS, G 2018 *Plasma Physics and Controlled Fusion* **60**, 064001.

- ROBEY, HF 2004 Effects of viscosity and mass diffusion in hydrodynamically unstable plasma flows. *Physics of plasmas* **11** (8), 4123–4133.
- SAMTANEY, RAVI 2003 *Physics of Fluids* **15**, L53–L56.
- SANO, TAKAYOSHI, INOUE, TSUYOSHI & NISHIHARA, KATSUNOBU 2013 *Physical review letters* **111**, 205001.
- SANO, TAKAYOSHI, NISHIHARA, KATSUNOBU, MATSUOKA, CHIHIRO & INOUE, TSUYOSHI 2012 *The Astrophysical Journal* **758**, 126.
- SANO, TAKAYOSHI, TAMATANI, SHOHEI, MATSUO, KAZUKI, LAW, KING FAI FARLEY, MORITA, TAICHI, EGASHIRA, SHUNSUKE, OTA, MASATO, KUMAR, RAJESH, SHIMOGAWARA, HIROSHI, HARA, YUKIKO & OTHERS 2021 Laser astrophysics experiment on the amplification of magnetic fields by shock-induced interfacial instabilities. *Physical Review E* **104** (3), 035206.
- SHAN, L. Q., WU, F. J., YUAN, Z. Q., WANG, W. W., CAI, H. B., TIAN, C., ZHANG, F., ZHANG, T. K., DENG, Z. G., ZHANG, W. S., TENG, J., BI, B., YANG, S. Q., YANG, D., ZHOU, W. M., GU, Y. Q., ZHANG, B. H. & ZHU, S. P. 2021 *High Power Laser and Particle Beams* **33**, 012004.
- SOFONEA, V, LAMURA, A, GONNELLA, G & CRISTEA, A 2004 Finite-difference lattice boltzmann model with flux limiters for liquid-vapor systems. *Physical Review E* **70** (4), 046702.
- SOFONEA, VICTOR & SEKERKA, ROBERT F 2003 Viscosity of finite difference lattice boltzmann models. *Journal of Computational Physics* **184** (2), 422–434.
- SUCCI, SAURO 2001 *The lattice Boltzmann equation: for fluid dynamics and beyond*. Oxford university press.
- TAPINO, KC, WHEATLEY, VINCENT, BOND, D & JAHN, I 2023 The effect of collisions on the multi-fluid plasma richtmyer–meshkov instability. *Physics of Plasmas* **30** (2), 022707.
- VIDAL, F, MATTE, JP, CASANOVA, M & LARROCHE, O 1993 *Physics of Fluids B: Plasma Physics* **5**, 3182–3190.
- WAGNER, ALEXANDER J & YEOMANS, JM 1998 Breakdown of scale invariance in the coarsening of phase-separating binary fluids. *Physical Review Letters* **80** (7), 1429.
- WANG, LIFENG, YE, WENHUA, HE, XIAN TU, WU, JUNFENG, FAN, ZHENG FENG, XUE, CHUANG, GUO, HONG YU, MIAO, WENYONG, YUAN, YONG TENG, DONG, JIA QIN & OTHERS 2017 Theoretical and simulation research of hydrodynamic instabilities in inertial-confinement fusion implsions. *Science China Physics, Mechanics & Astronomy* **60**, 1–35.
- WANG, YONG, ZHONG, CHENGWEN, CAO, JUN, ZHUO, CONGSHAN & LIU, SHA 2020 *Computers & Mathematics with Applications* **79**, 1590–1618.
- WHEATLEY, V, PULLIN, DI & SAMTANEY, R 2005a *Journal of Fluid Mechanics* **522**, 179–214.
- WHEATLEY, VINCENT, PULLIN, DI & SAMTANEY, R 2005b *Physical review letters* **95**, 125002.
- WHEATLEY, VINCENT, SAMTANEY, R & PULLIN, DI 2009 *Physics of Fluids* **21**, 082102.
- WHEATLEY, V, SAMTANEY, RAVI, PULLIN, DI & GEHRE, RM 2014 *Physics of Fluids* **1**, 016102.
- XU, AIGUO, CHEN, JIE, SONG, JIAHUI, CHEN, DAWEI & CHEN, ZHIHUA 2021a Progress of discrete boltzmann study on multiphase complex flows. *Acta Aerodyn.Sin* **39** (3), 138–169.
- XU, AIGUO, JIAHUI, SONG, FENG, CHEN, KAN, XIE & YANGJUN, YING 2021b *Chinese Journal of Computational Physics* **38**, 631.
- XU, AIGUO, LIN, CHUANDONG, ZHANG, GUANGCAI & LI, YINGJUN 2015 *Physical Review E* **91**, 043306.
- XU, AIGUO, SHAN, YI MING, CHEN, FENG, GAN, YANBIAO & LIN, CHUANDONG 2021c Progress of mesoscale modeling and investigation of combustion multiphase flow. *Acta Aeronauticaet Astronautica Sinica* **42** (12), 46–62.
- XU, AIGUO, SONG, JIAHUI, CHEN, FENG, XIE, KAN & YING, YANGJUN 2021d Modeling and analysis methods for complex field sbased on phase space. *Chinese Journal of Computational Physics* **38** (6), 631–660.
- XU, AIGUO, ZHANG, GUANGCAI, GAN, YANBIAO, CHEN, FENG & YU, XIJUN 2012 *Frontiers of Physics* **7**, 582–600.

- XU, AIGUO, ZHANG, GUANGCAI, YING, YANGJUN & WANG, CHENG 2016 Complex fields in heterogeneous materials under shock: Modeling, simulation and analysis. *Science China Physics, Mechanics & Astronomy* **59**, 1–49.
- XU, A., ZHANG, G. & ZHANG, Y. 2018 Discrete Boltzmann Modeling of Compressible Flows. In *Kinetic Theory* (ed. G. Kyzas & A. Mitropoulos), chap. 02. Rijeka: InTech.
- XU, AIGUO & ZHANG, YUDONG 2022 *Complex Media Kinetics*, 1st edn. Science Press, Beijing.
- XU, KUN & HUANG, JUAN-CHEN 2010 A unified gas-kinetic scheme for continuum and rarefied flows. *Journal of Computational Physics* **229** (20), 7747–7764.
- YAN, XX, CAI, HB, YAO, PL, HUANG, HX, ZHANG, EH, ZHANG, WS, DU, B, ZHU, SP & HE, XT 2021 Ion kinetic effects on the evolution of richtmyer–meshkov instability and interfacial mix. *New Journal of Physics* **23** (5), 053010.
- YAO, PEI LIN, CAI, HONG BO, YAN, XIN XIN, ZHANG, WEN SHUAI, DU, BAO, TIAN, JIAN MIN, ZHANG, EN HAO, WANG, XUE WU & ZHU, SHAO PING 2020 *Matter and Radiation at Extremes* **5**, 054403.
- YE, HAIYAN, LAI, HUILIN, LI, DEMEI, GAN, YANBIAO, LIN, CHUANDONG, CHEN, LU & XU, AIGUO 2020 *Entropy* **22**, 500.
- ZHAI, ZHIGANG, SI, TING, LUO, XISHENG & YANG, JIMING 2011 On the evolution of spherical gas interfaces accelerated by a planar shock wave. *Physics of Fluids* **23** (8), 084104.
- ZHAI, ZHIGANG, ZOU, LIYONG, WU, QIANG & LUO, XISHENG 2018 Review of experimental richtmyer–meshkov instability in shock tube: from simple to complex. *Proceedings of the Institution of Mechanical Engineers, Part C: Journal of Mechanical Engineering Science* **232** (16), 2830–2849.
- ZHANG, DEJIA, XU, AIGUO, ZHANG, YUDONG, GAN, YANBIAO & LI, YINGJUN 2022a Discrete boltzmann modeling of high-speed compressible flows with various depths of non-equilibrium. *Physics of Fluids* **34** (8), 086104.
- ZHANG, HUAN-HAO, ZHENG, CHUN, AUBRY, NADINE, WU, WEI-TAO & CHEN, ZHI-HUA 2020 Numerical analysis of richtmyer–meshkov instability of circular density interface in presence of transverse magnetic field. *Physics of Fluids* **32** (11), 116104.
- ZHANG, SHENG-BO, ZHANG, HUAN-HAO, CHEN, ZHI-HUA & ZHENG, CHUN 2023 Suppression mechanism of richtmyer–meshkov instability by transverse magnetic field with different strengths. *Physics of Plasmas* **30** (2), 022107.
- ZHANG, YUDONG, XU, AIGUO, CHEN, FENG, LIN, CHUANDONG & WEI, ZON-HAN 2022b *AIP Advances* **12**, 035347.
- ZHANG, YUDONG, XU, AIGUO, ZHANG, GUANGCAI, CHEN, ZHIHUA & WANG, PEI 2019a Discrete boltzmann method for non-equilibrium flows: Based on shakhov model. *Computer Physics Communications* **238**, 50–65.
- ZHANG, YUDONG, XU, AIGUO, ZHANG, GUANGCAI, GAN, YANBIAO, CHEN, ZHIHUA & SUCCI, SAURO 2019b *Soft matter* **15**, 2245–2259.
- ZHANG, YUDONG, XU, AIGUO, ZHANG, GUANGCAI, ZHU, CHENGMIN & LIN, CHUANDONG 2016 *Combustion and Flame* **173**, 483–492.
- ZHANG, YU-DONG, XU, AI-GUO, ZHANG, GUANG-CAI & CHEN, ZHI-HUA 2018 *Communications in Theoretical Physics* **69**, 77.
- ZHOU, YE 2017a *Physics Reports* **720-722**, 1–136.
- ZHOU, YE 2017b *Physics Reports* **723**, 1–160.
- ZHOU, YE, WILLIAMS, ROBIN JR, RAMAPRABHU, PRAVEEN, GROOM, MICHAEL, THORNBER, BEN, HILLIER, ANDREW, MOSTERT, WOUTER, ROLLIN, BERTRAND, BALACHANDAR, S, POWELL, PHILLIP D & OTHERS 2021 Rayleigh–taylor and richtmyer–meshkov instabilities: A journey through scales. *Physica D: Nonlinear Phenomena* **423**, 132838.